Focus Section: Arctic and Antarctic Seismology

Swell-Triggered Seismicity at the Near-Front Damage Zone of the Ross Ice Shelf

Richard C. Aster*[1], Bradley P. Lipovsky[2], Hank M. Cole[1], Peter D. Bromirski[3], Peter Gerstoft[3], Andrew Nyblade[4], Douglas A. Wiens[5], and Ralph Stephen[6]

Abstract

Ocean swell interacting with Antarctic ice shelves produces sustained (approximately, 2×10^6 cycles per year) gravity-elastic perturbations with deformation amplitudes near the ice front as large as tens to hundreds of nanostrain. This process is the most energetically excited during the austral summer, when sea ice-induced swell attenuation is at a minimum. A 2014–2017 deployment of broadband seismographs on the Ross Ice shelf, which included three stations sited, approximately, 2 km from the ice front, reveals prolific swell-associated triggering of discrete near-ice-front (magnitude $\gtrsim 0$) seismic subevents, for which we identify three generic types. During some strong swell episodes, subevent timing becomes sufficiently phase-locked with swell excitation, to create prominent harmonic features in spectra calculated across sufficiently lengthy time windows via a Dirac comb effect, for which we articulate a theoretical development for randomized interevent times. These events are observable at near-front stations, have dominant frequency content between 0.5 and 20 Hz, and, in many cases, show highly repetitive waveforms. Matched filtering detection and analysis shows that events occur at a low-background rate during all swell states, but become particularly strongly excited during large amplitude swell at rates of up to many thousands per day. The superimposed elastic energy from swell-triggered sources illuminates the shelf interior as extensional (elastic plate) Lamb waves that are observable more than 100 km from the ice edge. Seismic swarms show threshold excitation and hysteresis with respect to rising and falling swell excitation. This behavior is consistent with repeated seismogenic fracture excitation and growth within a near-ice-front damage zone, encompassing fracture features seen in satellite imagery. A much smaller population of distinctly larger near-front seismic events, previously noted to be weakly associated with extended periods of swell perturbation, likely indicate calving or other larger-scale ice failures near the shelf front.

Cite this article as Aster, R. C., B. P. Lipovsky, H. M. Cole, P. D. Bromirski, P. Gerstoft, A. Nyblade, D. A. Wiens, and R. Stephen (2021). Swell-Triggered Seismicity at the Near-Front Damage Zone of the Ross Ice Shelf, *Seismol. Res. Lett.* **XX**, 1–25, doi: 10.1785/0220200478.

Supplemental Material

Introduction

Ice shelves span, approximately, 45% of the Antarctic coastline. Importantly, they create restraining arch and grounding line stresses that slow the discharge of grounded ice sheets to the ocean, thus, mitigating glacial contributions to global sea level change. Some ice shelves have partially or totally collapsed in recent decades (e.g., Glasser and Scambos, 2008; Scambos *et al.*, 2009) and, most are presently experiencing thinning and mechanical weakening, driven by ocean warming and associated ocean current changes (Paolo *et al.*, 2015) and/or ocean and atmospheric warming (Banwell *et al.*, 2019). Ice shelves, and their associated ice sheets, are susceptible to a variety of atmospheric, oceanic, and solid Earth perturbations, including scenarios in which multiple destabilizing processes may reinforce (e.g., Barletta *et al.*, 2018; Pattyn and Morlighem, 2020). A poorly constrained perturbing influence on ice shelves is gravitationally and elastically propagated stress induced by ocean swell, which creates $\approx 2 \times 10^6$ strain cycles per year of widely varying amplitude at periods between about 8 and 30 s.

Theoretical studies of gravity-elastic modes of wave propagation in ice shelves were introduced by Press and Ewing

1. Geosciences Department, Warner College of Natural Resources, Colorado State University, Fort Collins, Colorado, U.S.A., https://orcid.org/0000-0002-0821-4906 (RCA); https://orcid.org/0000-0003-1684-9116 (HMC); 2. Department of Earth and Space Sciences, University of Washington, Seattle, Washington, U.S.A., https://orcid.org/0000-0003-4940-0745 (BPL); 3. Scripps Institution of Oceanography, University of California, San Diego, California, U.S.A., https://orcid.org/0000-0002-0471-062X (PG); 4. Department of Geosciences, Penn State University, University Park, Pennsylvania, U.S.A., https://orcid.org/0000-0002-6844-587X (AN); 5. Department of Earth and Planetary Sciences, Washington University, St. Louis, Missouri, U.S.A.; 6. Woods Hole Oceanographic Institution, Woods Hole, Massachusetts, U.S.A., https://orcid.org/0000-0003-0937-2049 (RS)

*Corresponding author: rick.aster@colostate.edu

© Seismological Society of America

Downloaded from http://pubs.geoscienceworld.org/ssa/srl/article-pdf/doi/10.1785/0220200478/5285507/srl-2020478.1.pdf
by Bradley Lipovsky

(1951), Press *et al.* (1951), and Holdsworth and Glynn (1978) introduced the hypothesis that ocean wave-induced stresses are contributors to calving and other fracture processes. Swell-induced ice shelf strain represents a teleconnection between the Antarctic ice sheet and distal (regional to ocean-basin-scale) regions of the meteorological and cryospheric system (e.g., MacAyeal *et al.*, 2006). In Antarctica, swell amplitudes at ice shelves are greatest during Austral summer periods, when swell interacts with the continent with minimal sea ice attenuation (Aster *et al.*, 2010; Massom *et al.*, 2018; Baker *et al.*, 2019; Hell *et al.*, 2019, 2020).

Glacial seismology is, particularly, notable for its ability to reveal short-time scale dynamic processes that are not resolvable via remote sensing, geodetic, and other methods. Tidewater Antarctic glacial termini and ice shelf systems as well as tabular icebergs are diversely and prolifically seismogenic (e.g., Nettles and Ekstrom, 2010; Bartholomaus *et al.*, 2015; Aster and Winberry, 2017; Winberry *et al.*, 2020). Studies spanning the past two decades have revealed a large number of ice-ocean (Okal and MacAyeal, 2006; MacAyeal *et al.*, 2006, 2009; Bromirski *et al.*, 2015, 2017; Chen *et al.*, 2018), ice-seabed (Martin *et al.*, 2010), and ice-ice (MacAyeal *et al.*, 2008, 2015) seismic sources. These studies have, additionally, observed a number of theoretically predicted but previously sparsely observed elastic wave phenomena within the firn, ice, ocean cavity, solid Earth, and atmosphere (e.g., Bassis *et al.*, 2008; Cathles *et al.*, 2009; Zhan *et al.*, 2014; MacAyeal *et al.*, 2015; Diez *et al.*, 2016; Godin and Zabotin, 2016; Chen *et al.*, 2018, 2019; Chaput *et al.*, 2018; Baker *et al.*, 2019, 2020; Olinger *et al.*, 2019).

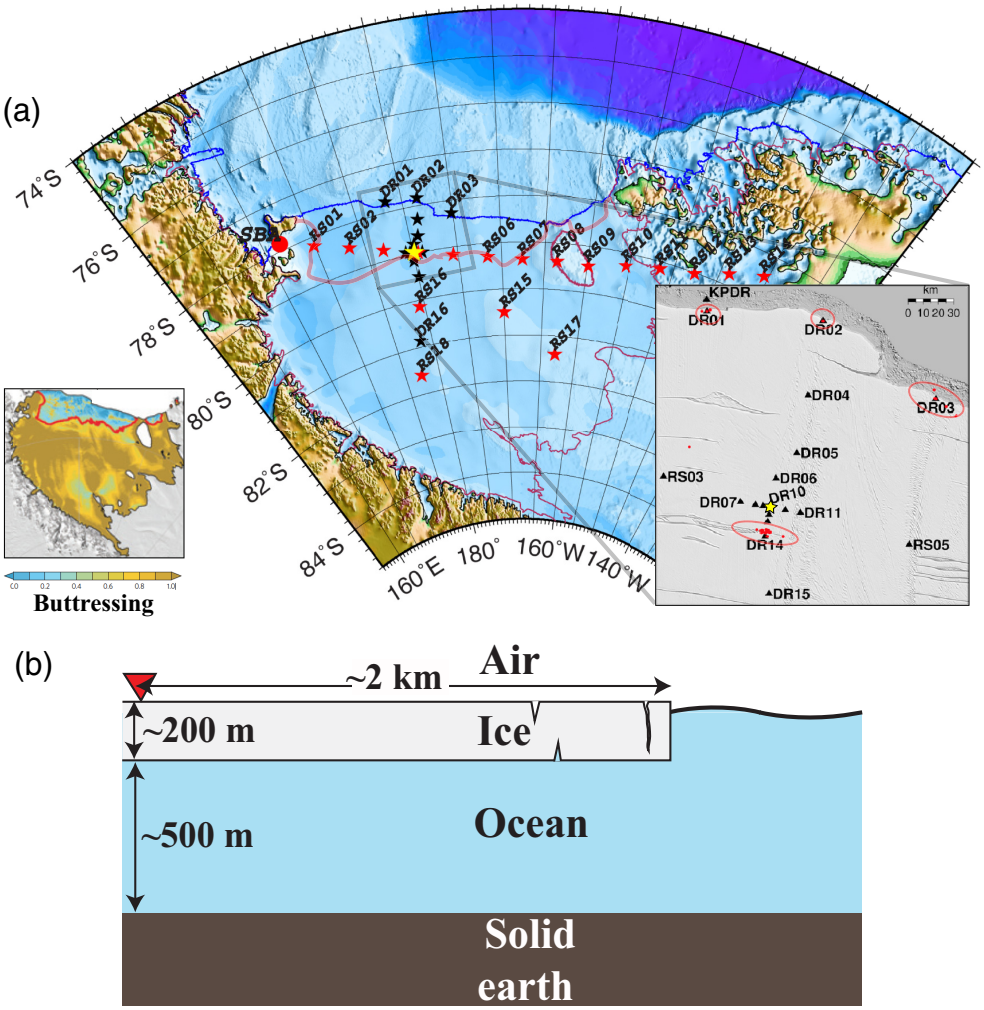

Figure 1. (a) Ross Ice Shelf (RIS-DRIS) deployment of broadband seismographs during November 2014–November 2016, with some stations recording as late as February 2017 (Bromirski *et al.*, 2015). Black and red stars indicate 200 and 100 samples per second continuously recording stations, respectively. The yellow star indicates central station DR10 near the Yesterday Field Camp. Geographic data are from Fretwell *et al.* (2013). The inset in right represents ice shelf morphology from Haran *et al.* (2018) showing source regions of high-amplitude ice shelf seismic events (red dots within elliptical regions) from Chen *et al.* (2019), including events near DR14 associated with intrashelf rift WR4 (Olinger *et al.*, 2019). KPDR is a pressure-sensor equipped ocean-bottom seismograph installed contemporaneously with the network (Chen *et al.*, 2019). Inset in the left represents degree of ice shelf stability critical buttressing estimated by Furst *et al.* (2016), with the (red) boundary transition also reproduced on the main figure. (b) Representative schematic geometry of the ice shelf edge in the vicinity of (red triangle) near-front seismic stations DR01, DR02, and DR03 (vertical–horizontal scale preserved). The color version of this figure is available only in the electronic edition.

The ice front region of a large shelf, such as the Ross Ice Shelf (RIS), might be presupposed to host a variety of seismic source processes due to geographically broad and continuous ocean forcing, progressive thinning, weakening, and ongoing mass loss near and at the terminus (e.g., Horgan *et al.*, 2011), and zones of heterogeneous strength and fracture (e.g., Scambos *et al.*, 2007; Olinger *et al.*, 2019). Remote studies and methods have noted associations between swell and

Downloaded from http://pubs.geoscienceworld.org/ssa/srl/article-pdf/doi/10.1785/0220200478/5285507/srl-2020478.1.pdf
by Bradley Lipovsky

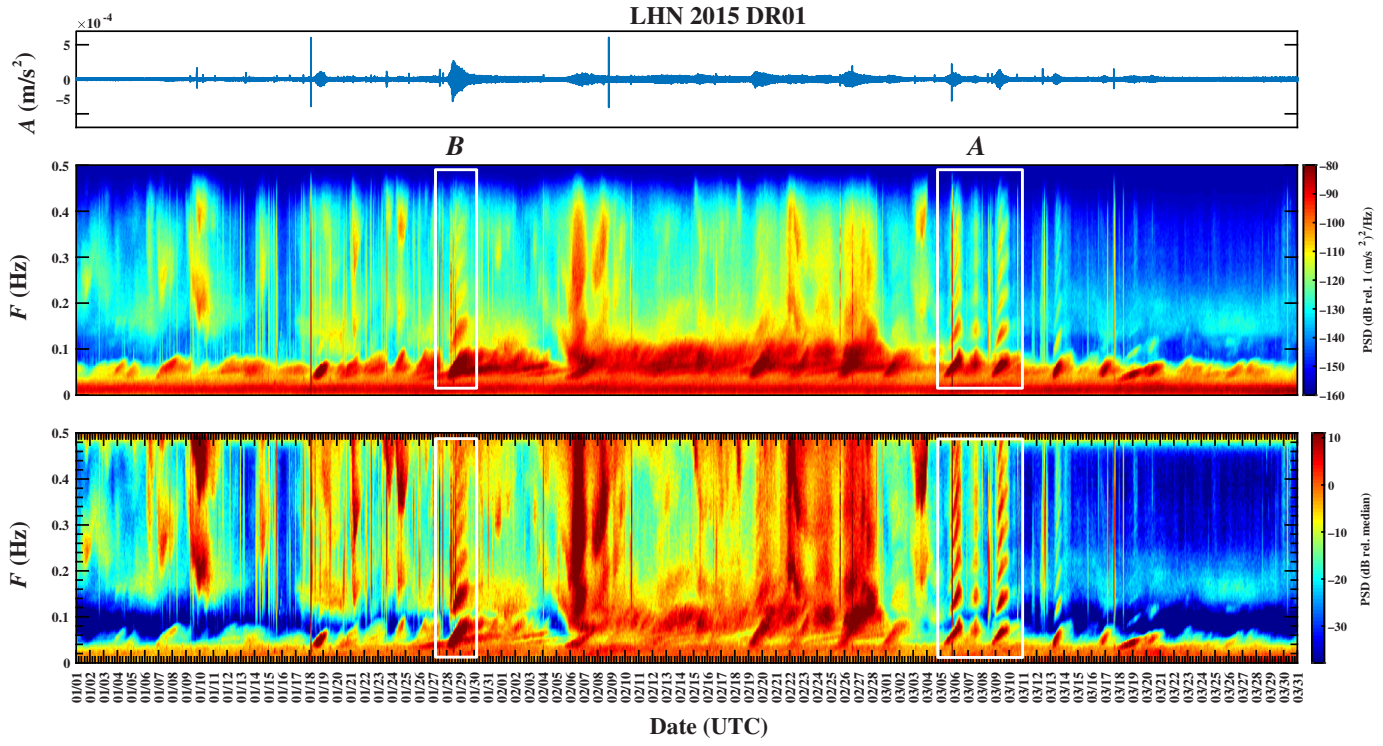

ice shelf fracture, using proxies for swell intensity (Banwell *et al.*, 2017), satellite imagery (Brunt *et al.*, 2011), and incorporating swell reanalysis products (Massom *et al.*, 2018). Here, we report seismographic observation of prolific swell-triggered seismicity in the near-ice-front region of the RIS, during a two-year broadband seismograph deployment (Fig. 1), focusing on the low sea-ice months of 2015, when the phenomenon is especially robust. Seismic stations incorporated Global Positioning System timing and three-component broadband 120 s corner period seismometers (Nanometrics T120PHQ) buried, approximately, 1.5 m below the firn surface and cabled to data logging (Quanterra Q330) and power systems installed within insulating boxes. Power was supplied by solar panels during the summer and by single-use low-temperature lithium thionyl chloride batteries during winter, providing year-round continuous operation with Iridium state-of-health telemetry. The signals that we describe and analyze are the most readily observed at the three near-front stations—DR01, DR02, and DR03. These stations were sited at respective distances of 2020, 1640, and 1700 m from the ice edge. The ice and ocean layer thicknesses at the three sites have been independently estimated, using seismic resonance (Baker *et al.*, 2020) and ice-penetrating radar and associated measurements from Ross Ocean and ice Shelf Environment and Tectonic setting Through Aerogeophysical surveys and modeling (ROSETTA)-Ice airborne geophysics studies Das *et al.* (2020). The corresponding ice thickness estimates for DR01, DR02, and DR03 are (212, 237), (169, 115), and (220, 241) m, respectively, and the underlying ocean column thicknesses were estimated to be (489, 466), (532, unestimated), and (316, 299) m, respectively. DR01 and DR03 were sited on contiguous sections of the ice shelf, but DR02 is sited atop Nascent iceberg, so named in reference to the ≈50 km long sea-connected rift to its south that may eventually result in the calving of an, approximately, 50 × 30 km tabular iceberg at this site (Cathles *et al.*, 2009). The near-front stations were sited, approximately, 120 km seaward of the critical buttressing contour for the ice shelf that regulates its ability to restrain landward glacial flow [(Furst *et al.*, 2016); Fig. 1].

Figure 2. North-component acceleration seismogram and spectrograms for representative near-ice-front station DR01 (Fig. 1) during low-sea ice periods (Chen *et al.*, 2019) between UTC 01 January and 31 March 2015. The upper spectrogram corresponds to the acceleration power spectral density (PSD, dB relative to $1(m/s^2)^2/Hz$). The lower differential spectrogram shows the deviation from the median PSD. Signals from primarily Southern Ocean swell energy (with approximate source ranges that are inversely proportional to df/dt; equation 1) appear prominently between ≈0.03 and 0.12 Hz. Also note the excitation of higher-frequency energy during many swell episodes. White boxes highlight particularly well-developed swell harmonic excitation during 5–11 March (expanded in Fig. 3). The color version of this figure is available only in the electronic edition.

Data and Methods

Frequency-domain observations

The long-period displacements of an ice shelf are dominated by swell (≈0.03–0.12 Hz) to infragravity (≈0.003–0.03 Hz) wave excitation (Bromirski *et al.*, 2010), with energy

Downloaded from http://pubs.geoscienceworld.org/ssa/srl/article-pdf/doi/10.1785/0220200478/5285507/srl-2020478.1.pdf
by Bradley Lipovsky

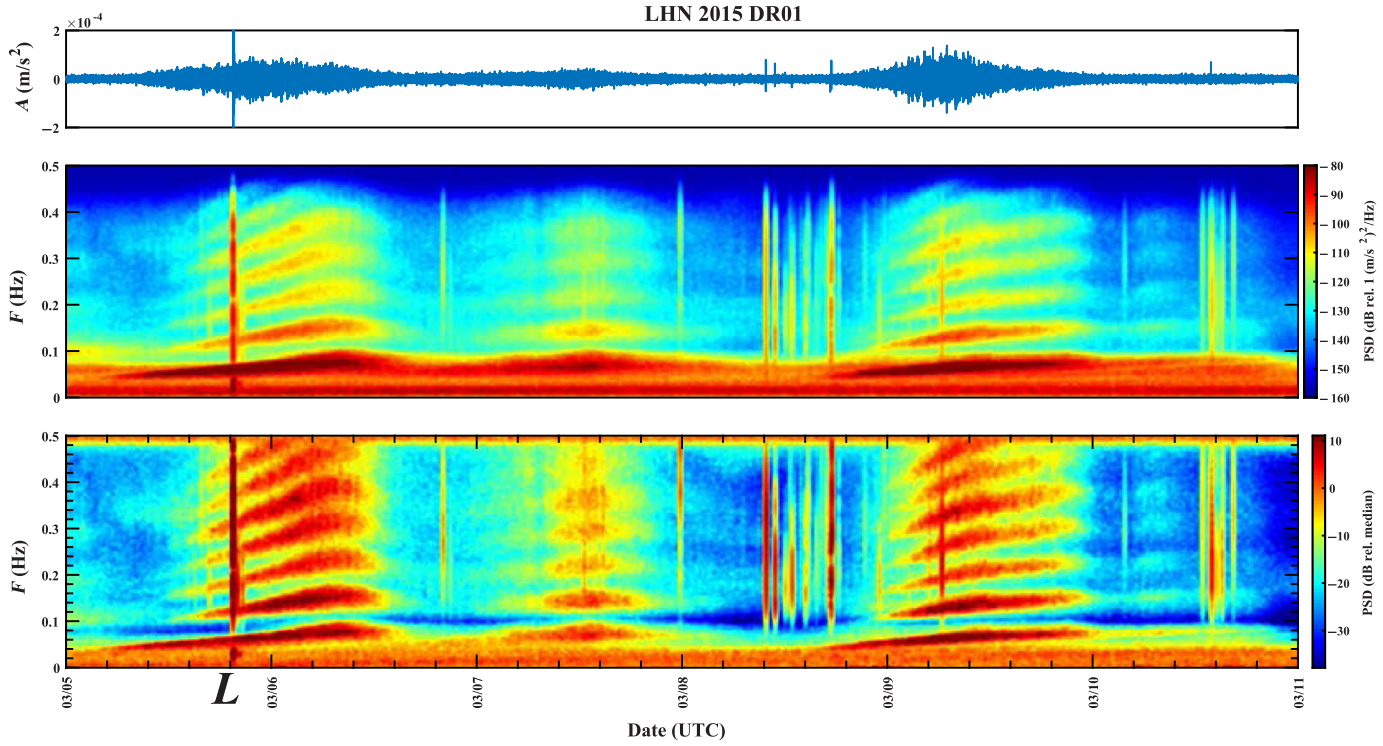

Figure 3. North-component DR01 north-component acceleration seismograms and spectrograms for three notable harmonic events that occurred during 5–11 March 2015 (highlighted period in Fig. 2). Application of equation (1) to the slope of the fundamental harmonic indicates a causative storm great-circle distance Δ, for these three events in the range of 1500–2000 km. Note the delayed onset of the appearance of swell harmonics by several hours, indicative of a swell excitation threshold for harmonic excitation relative to the (fundamental) swell signal in all three instances. Note also a superimposed and characteristic excitation in the infragravity waveband near 0.0125 Hz (80 s period) that occurs year-round in much of the Southern Ocean (e.g., Fig. 2; Godin *et al.*, 2013; Baker *et al.*, 2019). *L* indicates the signal associated with a large RIS front icequake (Fig. 6). The color version of this figure is available only in the electronic edition.

propagating from the ice edge into the shelf interior as elastic and gravity-elastic waves (Okal and MacAyeal, 2006; Bromirski *et al.*, 2015; Baker *et al.*, 2019; Chen *et al.*, 2019). Figure 2 shows a three-month acceleration power spectral density (PSD) spectrogram observed at RIS near-ice-edge station DR01 from the RIS-Dynamic Ross Ice Shelf (DRIS) experiment (Fig. 1; Bromirski *et al.*, 2015). A notable spectral feature is prominent and recurring power at frequencies above the swell band between, approximately, 0.12 and 0.5 Hz. During some episodes of swell excitation, a harmonic spectral structure appears in spectrograms characterized by integer multiple harmonics that proportionately "glide" in frequency with the incident swell excitation. These harmonic episodes occur the most prominently during the annual low sea ice period (e.g., Anthony *et al.*, 2015; Baker *et al.*, 2019; Chen *et al.*, 2019) between, approximately, December and March (Figs. 2–4), during which the ice shelf edge may become maximally exposed to incoming swell. We focus here on representative signals associated with the harmonic phenomenon during the first 90 days of 2015 (1 January–31 March), but this behavior is also observed during 2016 (Fig. B1, available in the supplemental material to this article).

Seismic data collected near the edge of an ice shelf or atop a tabular iceberg tracks the ocean swell (MacAyeal *et al.*, 2006; Cathles *et al.*, 2009) show a strong swell-associated energy peak, as floating ice buoyantly and elastically responds to ocean gravity waves. The distances to the causative storm sources can be estimated (e.g., Haubrich *et al.*, 1963; Okal and MacAyeal, 2006; Hell *et al.*, 2019, 2020) from the dispersion of the seismic signal using the deep water gravity wave equation:

$$\Delta = \frac{g}{4\pi}\left(\frac{df}{dt}\right)^{-1}, \tag{1}$$

in which df/dt is the dispersed slope of the seismically or otherwise observed swell episode (e.g., as measured from a spectrogram), and g is the gravitational acceleration. The manifestation of harmonics is accompanied by nonharmonic higher frequency energy up to tens of hertz (Fig. B2, available in the supplemental material). Harmonics are the most prominently observed at near-ice-front stations DR01, DR02, and DR03, but are, to a lesser extent, also observed at interior shelf stations exceeding 100 km from the ice edge (Fig. B3, available in the supplemental material).

Downloaded from http://pubs.geoscienceworld.org/ssa/srl/article-pdf/doi/10.1785/0220200478/5285507/srl-2020478.1.pdf
by Bradley Lipovsky

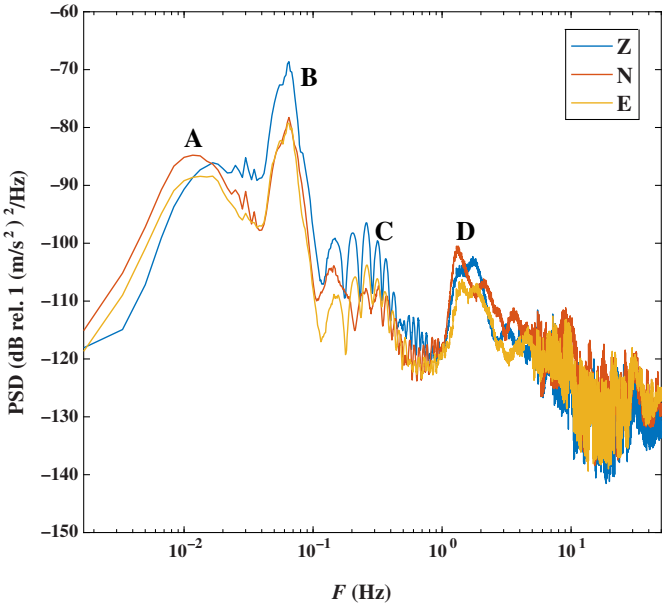

Figure 4. Long-term (48 hr) acceleration PSD of the 5–6 March 2015 (type *A* subevent-dominated) swell harmonic episode (the initial episode in the spectrogram of Fig. 3) for the three native (Z, N, E) seismic components at station DR01. Prominent spectral features: (A) infragravity waves; (B) swell band; (C) swell harmonics; (D) high-frequency subevents. PSDs were estimated using Welch's method ensemble averaging, using 50% overlapping 10 min (120,000-point) Hamming windows. The color version of this figure is available only in the electronic edition.

The occurrence of harmonics and other higher frequency seismic energy indicates a generic nonlinearity in the response of the ice shelf to the narrowband swell excitation. Generally, this may result from either strong, continuously nonlinear stress–strain behavior and/or from the excitation of swell phase-locked secondary subevents with differing frequency content.

Time-domain observations

Time-domain velocity seismograms in the swell (0.03–0.12 Hz) and high-frequency (predominantly >0.5 Hz) bands reveal that intervals of swell harmonic excitation are associated with the occurrence of similar impulsive subevents occurring at rates of up to many thousands per day. Figure 5 shows this phenomenon using a representative swell (0.03–0.12 Hz) and high-frequency (0.5–5 Hz) band-filtered seismograms recorded at station DR01 during a 9 min time segment beginning at 22:00 UTC on 5 March 2015. Many individual subevents are low signal-to-noise and/or overlapping, but their generally similar waveforms allow us to readily extract and analyze them further. We unbiasedly detect, extract, and characterize the subevents by: (1) peak amplitude detection of high-frequency (>0.5 Hz) transient signals; (2) robust stacking of the peak-detected events found in step (1) across long (up to multiday) time intervals to produce a matched filter template; (3) moving-window correlation redetection of events using templates from step (2) across long duration (up to months) time-series segments.

We applied this automated detector to one-day to multiday velocity seismic data for the first 90 days of 2015 (Fig. 2). For the peak detection step (1), we applied an initial $+6\sigma$ peak amplitude criterion and peak-to-peak minimum time separation of 4 s. If this criterion was insufficient to detect 200 or more prospective subevents, the amplitude threshold was progressively reduced in increments of 0.1σ, until 200 or more potential subevent detections were acquired (thus, increasing the likelihood of extracting potential lower amplitude and/or lower signal-to-noise subevents during less active periods). Extracted data segments of about 12 s duration were centered on peak amplitudes and robustly stacked, preserving the true amplitude of each contributing seismogram. Events from the peak detection population, with amplitudes exceeding 3σ of the above selected population, were omitted from this stacking procedure, because they were found to constitute a distinct population of higher magnitude events associated with more complex seismograms (Fig. 6). These larger magnitude near-front RIS events are sufficiently energetic and coupled to the subshelf cavity, to produce seismic signals that propagate within the ocean column and solid Earth, and can be tracked in RIS-DRIS network record sections. Chen *et al.* (2019) attributed these events to larger calving, intrashelf fracturing, and/or basal crevasse expansion events, while, noting that these large events were loosely correlated with strong swell intervals, including, approximately, 70% of the time for events during the austral summer period of 2015.

The robust stacking algorithm that we employ identified waveforms for which the 2-norm difference of the energy-normalized event seismogram with respect to the median stack of all such waveforms was within the 25% quantile, thus, ensuring similarity and coherent stacking. We found that this algorithm produced consistent representations of the highest signal-to-noise subevent types within these characteristic seismogram populations without strong sensitivity to the specific quantile threshold, provided it was less than, approximately, 40%. Finally, selected events identified by the robust stacking algorithm were linearly stacked, with their true amplitudes (meters per second) preserved to produce representative seismograms across daily or other seismogenic intervals. For extended time periods, typical of distinct swell episodes from individual storms (typically spanning 1–2 calendar days), we extracted, cataloged, and analyzed template-detected events with moving-window correlation coefficients that exceeding $+3\sigma$ of the correlation function standard deviation in computing representative robust waveform stacks.

We demonstrate the general behavior of these swell-induced subevent swarms, using a prominent harmonic episode from 5–6 March 2015, with continuous 48 hr 200 samples per second seismic velocity data from DR01 (Fig. 1 and Fig. B2,

Downloaded from http://pubs.geoscienceworld.org/ssa/srl/article-pdf/doi/10.1785/0220200478/5285507/srl-2020478.1.pdf
by Bradley Lipovsky

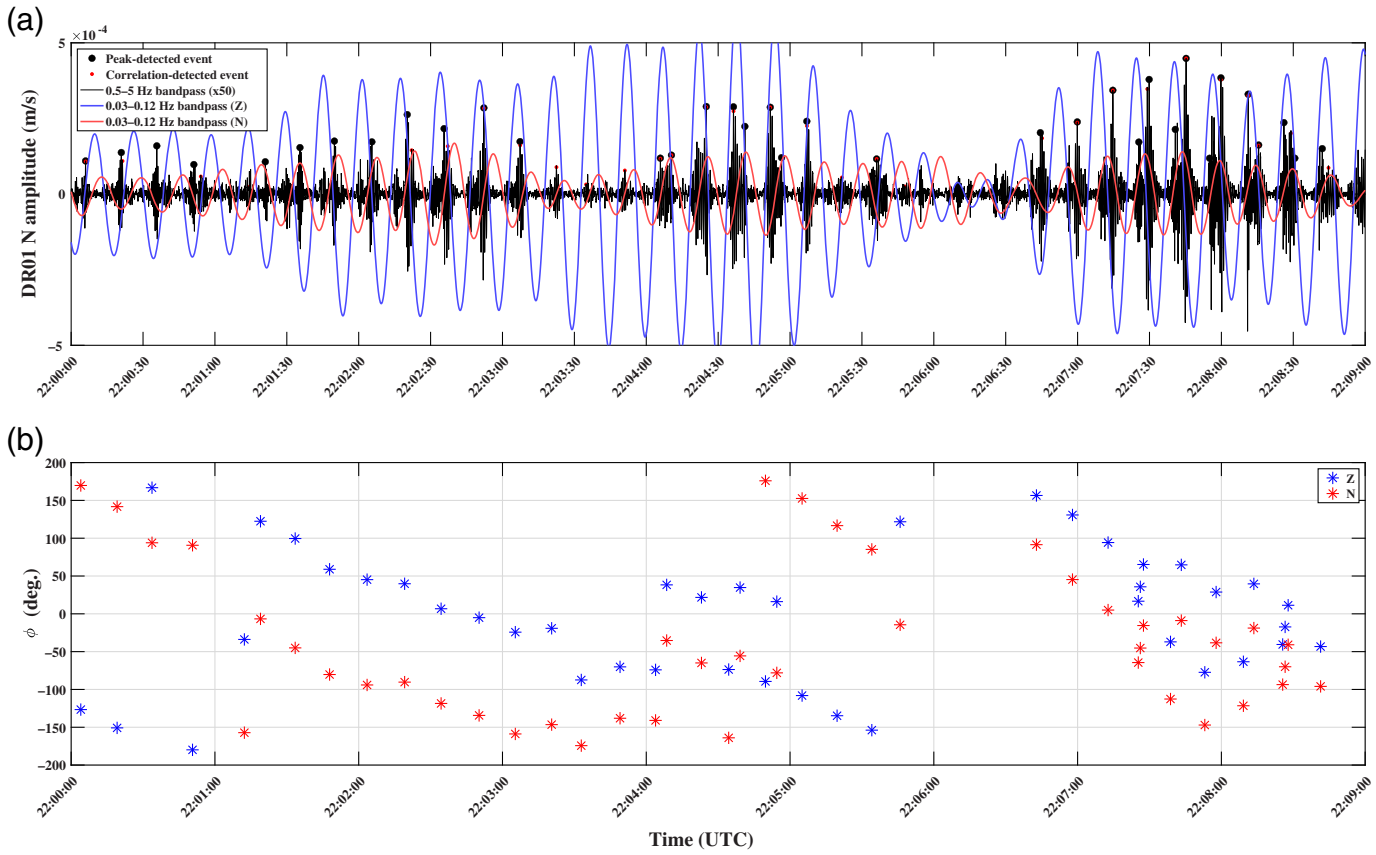

Figure 5. (a) Velocity (9 min duration) seismograms recorded at station DR01 during a representative harmonic episode beginning at 22:00 UTC on 5 March 2015 (Fig. 2). Blue and red traces indicate swell-band signal (0.03–0.12 Hz) for the vertical and north components, respectively. Black traces indicate subevent north-component signal (0.5–5 Hz; magnified in amplitude by a factor of 50 for visibility). Subevents were initially detected using peak amplitude detection in this band (black dots). Correlation (matched filter) detection with stack-derived templates produces additional event detections (red dots). (b) Corresponding instantaneous swell phase during this interval for jointly detected peak-detected and correlation-detected subevent onset times (with onset approximated as a 2 s correction relative to the peak detection times shown at top). The phase difference between the vertical and north components is typically approximately 90°, representing retrograde elliptical motion in the swell band for propagation toward the ice shelf interior (Chen *et al.*, 2018). Interevent times tend to statistically track swell, but with a substantially random phase relationship (Figs. B4 and B11, available in the supplemental material). The color version of this figure is available only in the electronic edition.

available in the supplemental material). For north-component seismic data (commonly, the maximum amplitude seismic component), this resulted in 4481 distinct moving window correlation detections for which the correlation function $C(t)$ exceeded 3σ ($3\sigma = 0.424$, in this example). Prolific matched filter detection of the majority of amplitude-detected peaks (3427), and of many smaller amplitude and lower signal-to-noise or overlapping subevents, is indicative of similar waveforms within the swell-associated seismic swarm (Fig. 7). These characteristic events show evidence for a triggered behavior with respect to the swell amplitude, showing a delayed initiation of several hours and becoming predominantly active at later times (Fig. 7 and Fig. B2, available in the supplemental material).

The approximate phase-locking of subevents shows typical event-to-event drifts, with respect to the swell-band seismic signal phase of ≈ – 10° or more (e.g., Fig. 5). The overall statistical timing and swell phase subevent alignment, throughout the example episode, is shown using 4 hr window histograms in Figures B4 and B5, available in the supplemental material. The quasiperiodic occurrence of secondary seismic sources, in approximate phase alignment with the swell signals, produces the observed harmonic spectral features via the Dirac comb effect (see Appendix) for sufficiently long-time windows that encompass a large number of swell cycles. The Dirac comb effect is a reference to the general appearance of spectral lines in time series that feature repeated subevents with a sufficient interevent timing consistence, such as, previously attributed in iceberg harmonic tremor (MacAyeal *et al.*, 2008; Martin *et al.*, 2010) and ice stream stick slip tremor (Lipovsky and Dunham, 2016).

Downloaded from http://pubs.geoscienceworld.org/ssa/srl/article-pdf/doi/10.1785/0220200478/5285507/srl-2020478.1.pdf
by Bradley Lipovsky

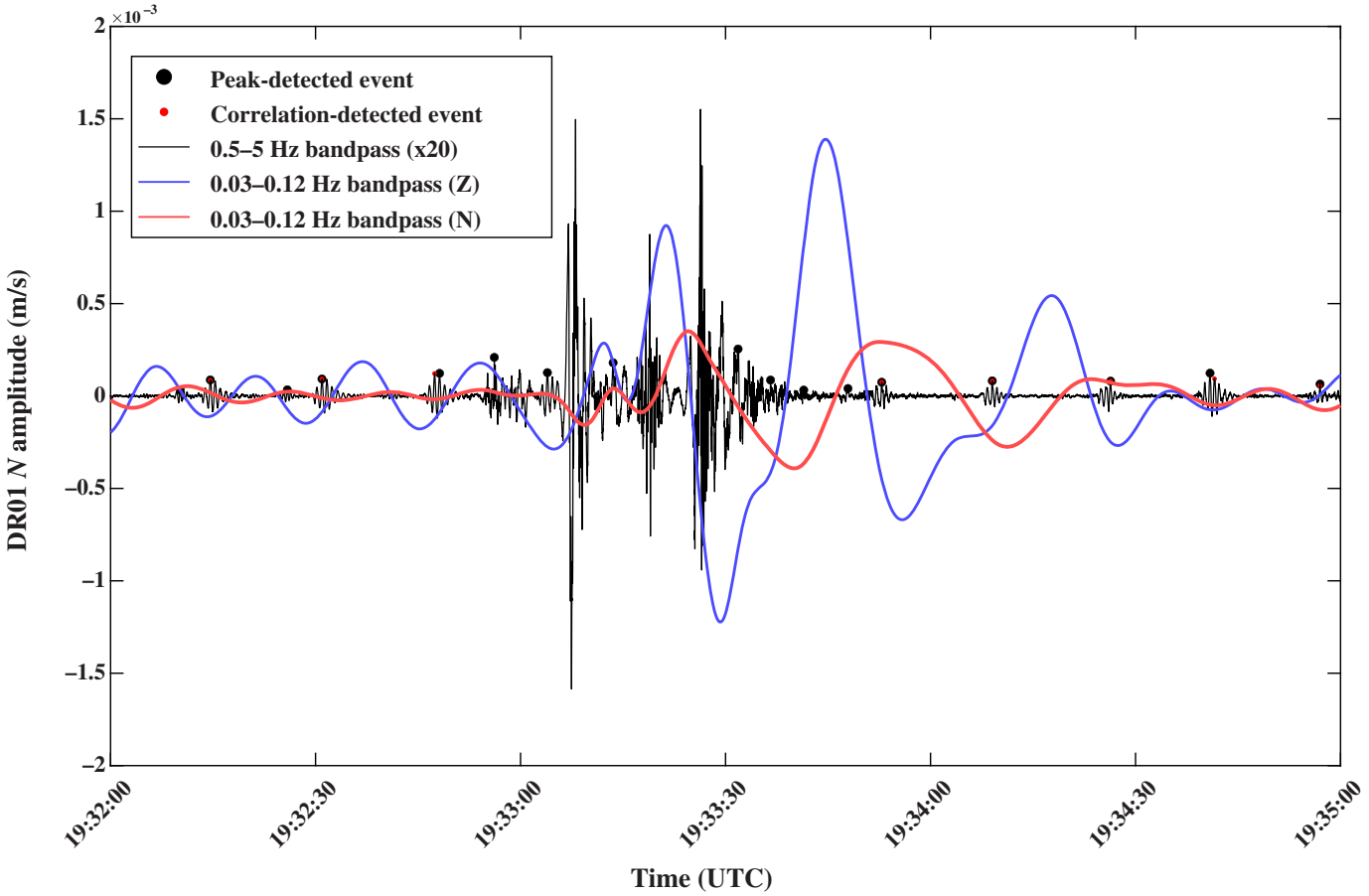

Figure 6. Representative (duration of 3 min) velocity seismograms at DR01 from the distinct population (Fig. 12) of larger near-front events (Chen *et al.*, 2019). Signals are presented in the manner of Figure 5 but using an amplitude scale that is four times larger. The event is prominently visible as a broadband transient occurring during the early phase (near 19:33 UTC on 5 March 2015) of the swell harmonic episode spectrogram shown in Figure 3 (event *L*), and in Figure B2, available in the supplemental material. The presence of multiple large subevents and a high-amplitude swell-band transient that initiates during the event sequence and persists for, approximately, 1 min. The small approximately swell phase-locked events visible at other times (identified with black dots) are type *A* subevents, which are dominant during this episode. The color version of this figure is available only in the electronic edition.

The time-dependent association between seismic energy in the swell and high-frequency bands for the 48 hr 5–6 March 2015 episode is displayed in Figure 8. Of particular note are a swell amplitude threshold near −85 dB (at approximately, 14:00 UTC on 5 March on the rising limb), above which high-frequency energy increases rapidly due to an increasing number and amplitude of subevents. The figure also shows a clockwise hysteresis loop due to this rising limb threshold effect, followed by subevent persistence to lower swell energy levels during the falling limb of the episode during 6 March.

Examining representative template stacked subevent seismograms for this and other swell episodes, we find evidence for, at least, three associated waveform types, all of which show retrograde sagittal plane dominant particle motion characteristic of Rayleigh waves propagating into the ice shelf interior from sources located between the near-ice-front stations and the ice front. Type *A* events (Figs. 5 and 9) are associated with the prominent 6 March episode and have a spectral peak near 1.4 s. Type *B* events are the most closely associated with an earlier year (28–29 January) and, particularly, energetic swell episode. Type *B* subevents are more broadband and include higher frequency peak spectral energy near 3–4 Hz (Fig. B6, available in the supplemental material). The clearest manifestations of types *A* and *B* harmonic subevent excitation are indicated in spectrogram of Figure 2. A third, type *C*, subevent category is also apparent on multiple days. Type *C* events are also narrowband and low frequency for such small events, and are distinguished by having a variable lower (often centered near 0.5 Hz) peak frequency and to be both time-symmetric and nonimpulsive. Time-domain inspection shows that extracted type *C* subevents, using our template extraction methodology, are actually high-amplitude segments of a continuous narrowband tremor (Fig. B7, available in the

Downloaded from http://pubs.geoscienceworld.org/ssa/srl/article-pdf/doi/10.1785/0220200478/5285507/srl-2020478.1.pdf
by Bradley Lipovsky

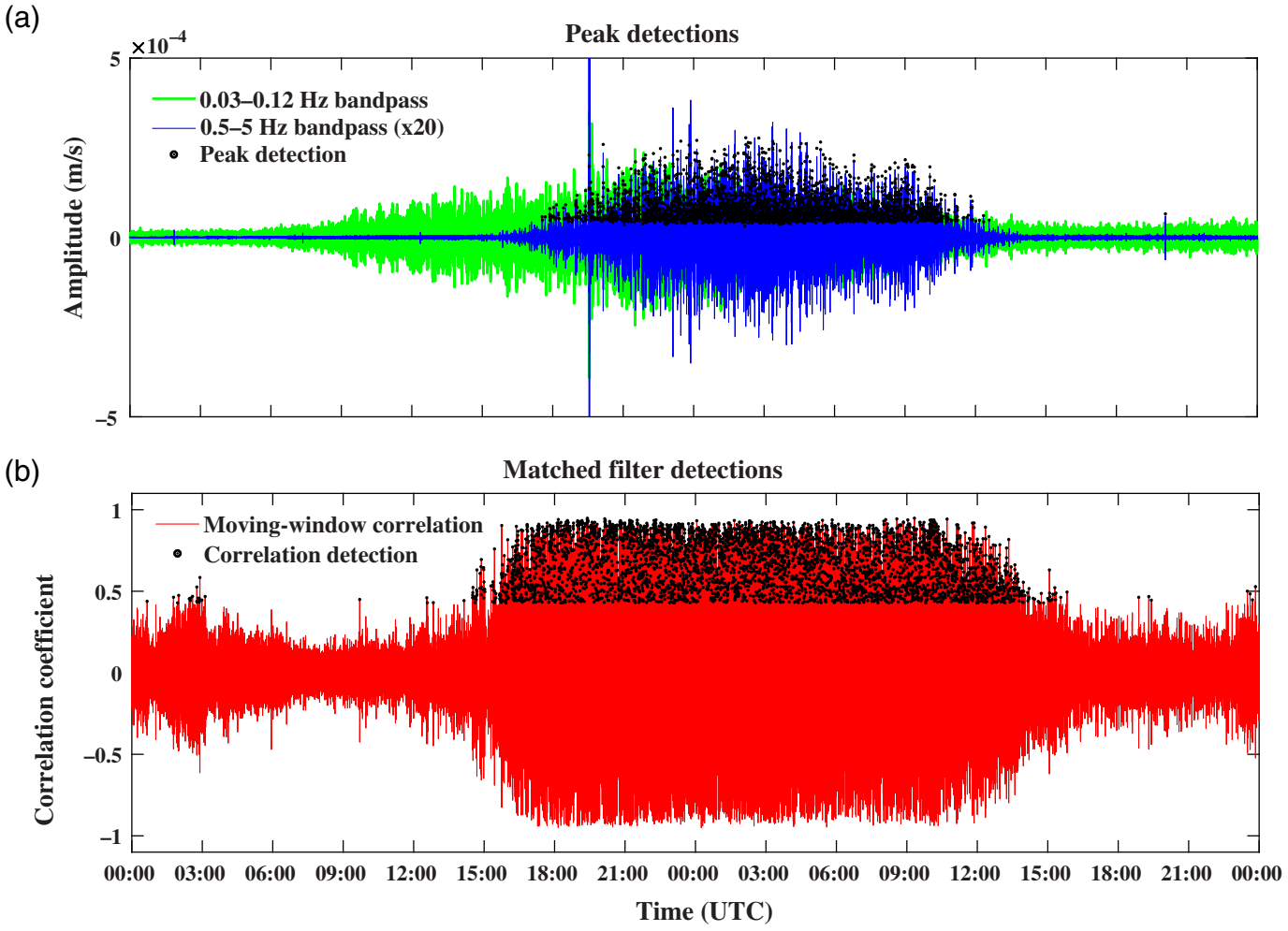

Figure 7. (a) Peak amplitude detections and seismograms (large outlying events removed from detection) during the 48 hr of 5–6 March 2015 spanning the harmonic episode shown in Figure B2 (available in the supplemental material). The peak detection algorithm used the north component of seismic velocity filtered between 0.5 and 5 Hz (blue) and detected 3628 events. The swell-band seismogram is also indicated in green. (b) Moving window correlation (red) and matched filter detections using a maximum amplitude-aligned template constructed from stacked peak-detected events shown at top, as described in the Time-domain observations section. During this time period, we found 3427 peak-detected and 4481 correlation-detected subevents; combining these produced a catalog of 5740 events. The unusually large event shown in Figure 6 near 19:33 UTC is also clearly visible, as is the (approximately, 9 hr) delayed onset of subevent activity, for example, with the delayed onset of harmonics observed in Figure 3. The color version of this figure is available only in the electronic edition.

supplemental material) and is observed at all three ice front stations. Their nature, thus, appears to differ from the impulsive types *A* and *B* activity; we note their occurrence here but focus the bulk of our analysis in this study on the impulsive and swell-triggered subevent types. Figure 4 shows predominant spectral peak near 1.2 Hz, for type *A* events from 5 to 6 March, and, peak near 4 Hz, for type *B* events, from 28 to 29 January. Particle motions, in both cases, are retrograde elliptical in the approximate north-vertical plane for northward propagation (Fig. 10), as expected for a horizontally propagating (Rayleigh-like) seismic wavefield.

Subevent magnitude estimation

A subevent magnitude range and distribution can be roughly estimated using a Lillie local magnitude formula employed by Olinger *et al.* (2019) for RIS internal rift-associated icequakes:

$$M_L = \log_{10}(A/T) + 2.76\log_{10}(D) - 2.48, \quad (2)$$

in which A is the maximum displacement amplitude in microns, T is the corresponding period of maximum displacement, and D is the source distance in kilometers. Maximum displacement amplitudes at DR01, during the 5–6 March 2015 episode, range between, approximately, 0.002 and 2 μm. We use a characteristic period of 1.2 s (Fig. 11) and a source distance corresponding to the mean ice edge distance ($D = 1.8$ km) for the three near-

Downloaded from http://pubs.geoscienceworld.org/ssa/srl/article-pdf/doi/10.1785/0220200478/5285507/srl-2020478.1.pdf
by Bradley Lipovsky

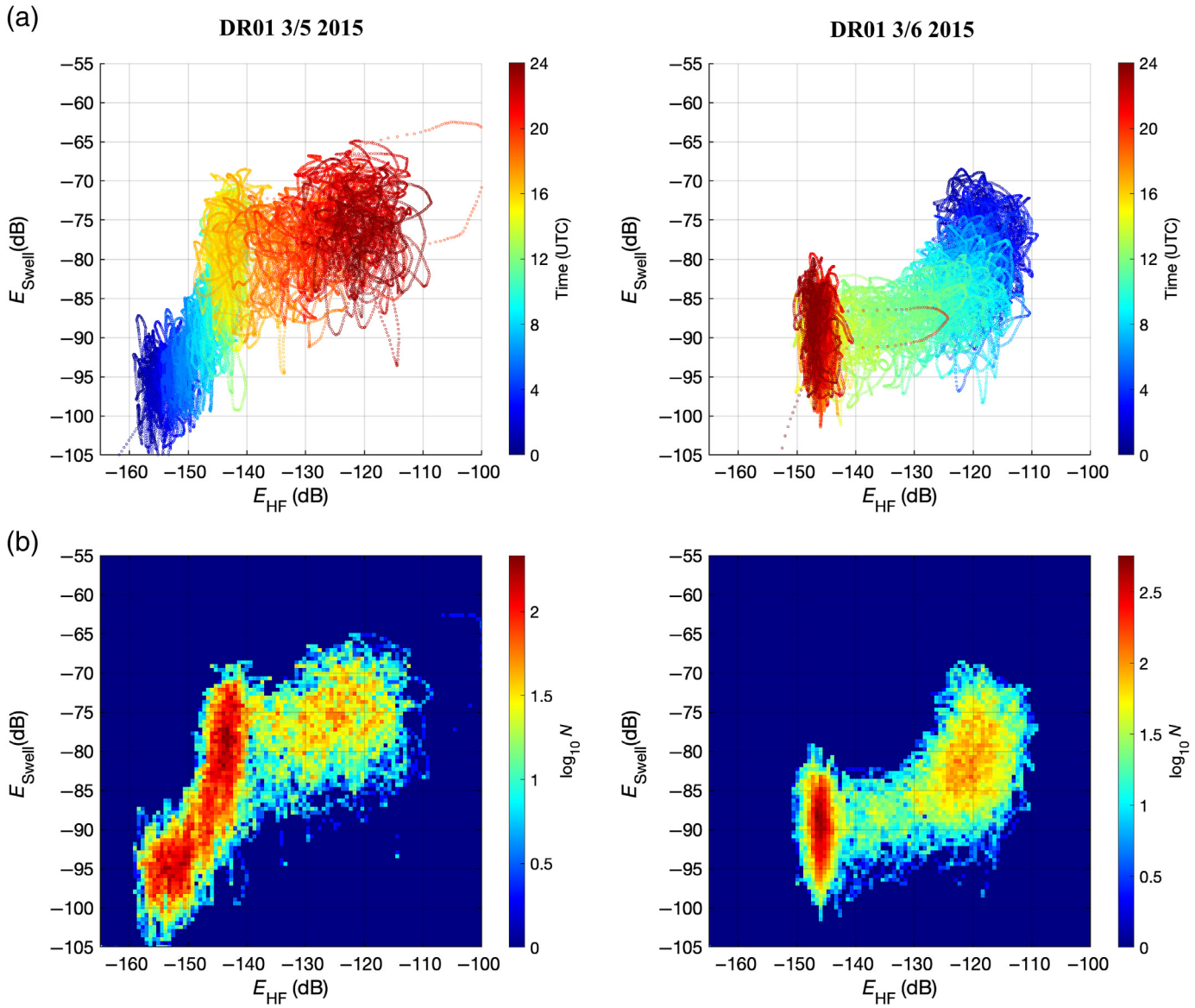

Figure 8. Swell (0.03–0.12 Hz; vertical velocity component) energy versus high-frequency (>0.5 Hz; north velocity component) energy evolution (dB) during the type *A* subevent-dominated 5–6 March 2015 harmonic episode. (a) Temporal evolution for days (left) 5 March and (right) 6 March, with data points colored by UTC hour. (b) Corresponding point densities. The midpoint of the swell episode occurs near 02:00 UTC on 6 March (Fig. B2, available in the supplemental material), so the two columns represent behavior during approximately rising and falling swell excitation of the ice shelf. Energy envelopes were calculated by convolving the squared time-domain amplitude signals in each band with a normalized 60 s Bartlett window and decimating each time series to 1 sample per second. Note the hysteresis evident in the differing trajectories between the rising and falling energy legs and the threshold excitation of strong high-frequency energy near a swell excitation level near –85 dB, corresponding to a velocity amplitude of ≈8.3×10^{-5} m/s or to a displacement of ≈2×10^{-4} m at a characteristic swell period of 15 s (Fig. B4, available in the supplemental material). The onset threshold effect for high-frequency energy is also apparent in an approximate 8 hr lag between the onset of high-frequency subevents and swell-band amplitude in Figure 7. The color version of this figure is available only in the electronic edition.

ice-front stations (DR01, DR02, and DR03; 2020, 1640, and 1700 m, respectively, constrained during deployment and from remote sensing images) and consistent with the near-front locations for large events determined by Chen *et al.* (2019) (Fig. 1). Event magnitudes are determined to be extremely small ($-2.6 < M_L < -0.8$) and ($-4 < M_L < -1.5$) for both the peak- and matched filter-detected subevent populations, respectively (Fig. 12). The magnitude distribution has a nonpower law shape (i.e., non-Gutenberg–Richter), with a mode near $M_L \approx -2.2$, and a very rapid fall-off at larger magnitudes. A small number

Downloaded from http://pubs.geoscienceworld.org/ssa/srl/article-pdf/doi/10.1785/0220200478/5285507/srl-2020478.1.pdf
by Bradley Lipovsky

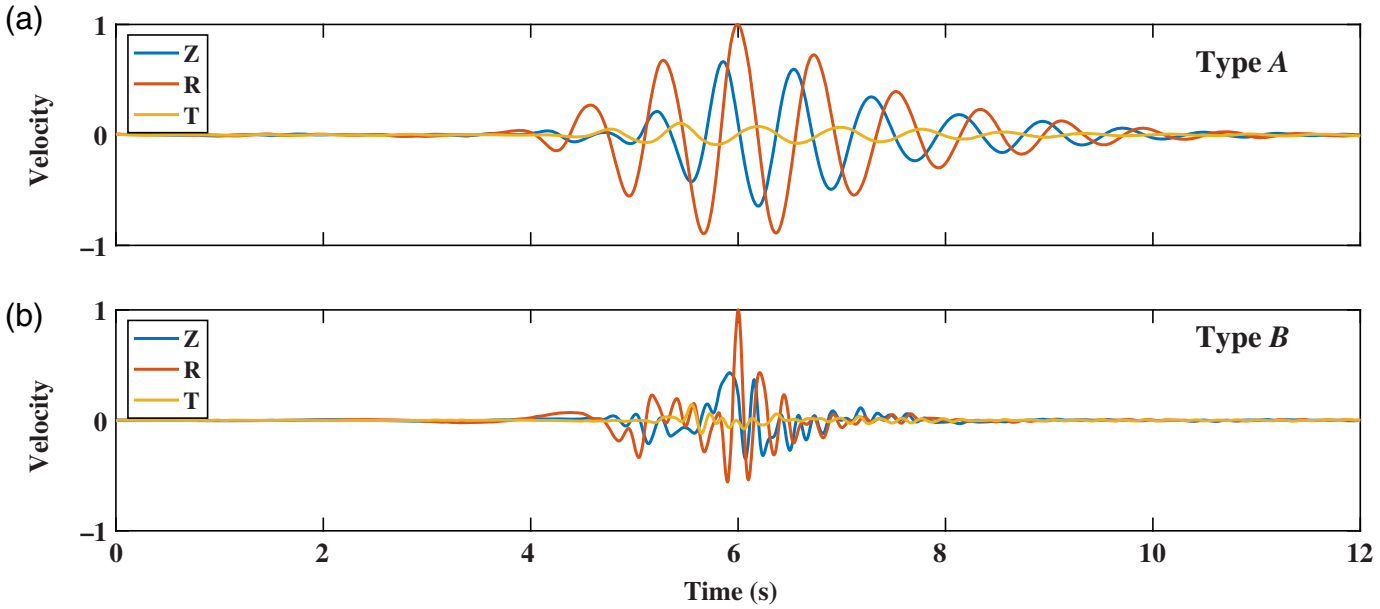

Figure 9. Amplitude-normalized three-component velocity stacked seismograms. (a) Type *A* repeating subevents during 5–6 March 2015 (Fig. 7); and (b) type *B* repeating subevents during 28–29 January 2015 recorded at station DR01. Horizontal components are rotated into radial (R) and tangential (T) components using variance tensor diagonalization of the full 12 s seismic signal. Although, the frequency content appreciably differs, the vast majority of the signal energy (≈98% and 95%, respectively) lies in the vertical–radial plane, and the radial direction points toward the closest ice edge (3.6° and 4.7° east of north, respectively). The color version of this figure is available only in the electronic edition.

of much larger events are distinct from the general distribution. Subevent seismograms, in the main population, are both low frequency, for events of this size, and narrowband (with a peak frequency content near 1.2 Hz; Fig. 4), when compared to fault-generated or brittle ice failure events. For comparison, a magnitude −2 tectonic earthquake (corresponding to an approximate seismic moment of 10^6 N · m (e.g., Hanks and Kanamori, 1979) observed in the absence of attenuation would have a typical corner frequency in the kilohertz range (e.g., Yamada *et al.*, 2007).

Subevent occurrence

We verified the persistent occurrence of swell-associated subevents on the RIS, throughout the low sea ice summer period, by applying our detection method to day-long time series at near-ice-front stations for 1 January–31 March 2015 (Fig. 2). Figure 13 shows three-component seismogram robust stacks for DR01 calculated on a UTC daily basis. The, approximately, 1.2 Hz center frequency narrowband type *A* subevent types observed during the 5–6 March 2015 episode are seen to occur, with some waveform and peak frequency variations, primarily later in this time period and variations in characteristic frequency. Figure 13 also highlights the occurrence on some days of the aforementioned second class of broader band type *B* subevents with higher frequency content (Fig. B8, available in the supplemental material) and by somewhat smaller amplitudes, and, thus, estimated magnitudes, assuming a similar near-ice-front origin (Fig. 12).

During 2015, type *B* events first appear in profusion around 28 January UTC, during the largest amplitude swell episode of 2015 observed for this region of the RIS. Stacked seismograms, hodograms, and spectra for a representative type *B* subevent are shown in Figures 9–11, respectively. The type *B* dominated swell episode is shown in detail in the 48 hr spectrogram of Figure B9, available in the supplemental material. Although, the waveforms appreciably differ between the two event types, type *B* subevents exhibit a similar hysteresis pattern of delayed onset and prolonged persistence with respect to swell excitation as type *A* episodes (Fig. B10, available in the supplemental material), and their approximate alignment with swell in phase and timing is similarly sufficient to result in spectrogram swell harmonics (Figs. B6, B11, and B12, available in the supplemental material). Daily subevent and swell polarization at DR01 is displayed in Figures 14–16. Although, polarization azimuth is generally stable, showing multiday variations on the scale of 10°, some low-amplitude subevent populations in late March develop a more east–west polarization (Figs. 14 and 15), as swell-band seismic polarization rotates to the northwest during this time period—a trend that is visible on all three stations (Figs. B13–B16, available in the supplemental material). These late season signals also show a narrowband type *A* character, but the center frequencies are notably higher (Fig. 13),

Downloaded from http://pubs.geoscienceworld.org/ssa/srl/article-pdf/doi/10.1785/0220200478/5285507/srl-2020478.1.pdf
by Bradley Lipovsky

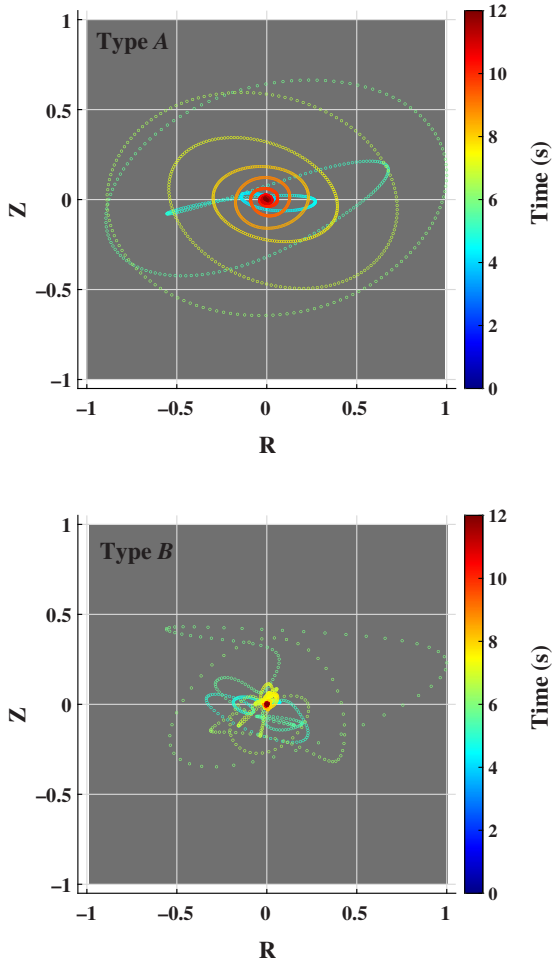

Figure 10. Z–R plane hodograms for the amplitude-normalized velocity subevent stacks shown in Figure 9. The color version of this figure is available only in the electronic edition.

and the polarization change may be influenced by the presence of the interior rift and the prominent north–south eastern edge of the partially detached Nascent iceberg segment of the RIS front (Fig. 1).

Intrashelf seismic illumination by high-frequency swell-triggered energy

Observations of subevents and harmonic spectra at all three near-front stations (DR01, DR02, and DR03) offer near-front observations of a swell-triggered subevent process that creates widespread seismic illumination along the ice-front shelf region and is observable at interior ice shelf stations to ranges exceeding 100 km (Fig. B3, available in the supplemental material). To examine this far-field wavefield, we utilized the subset of seismic stations DR04–DR13, along with RS04, which comprise an interior shelf array centered on DR10 with interstation distances ranging from approximately 5–90 km (Fig. 1). Signals from the prominent event of UTC day 6 March 2015 were band-pass filtered (four-pole zero phase Butterworth implementation) between 0.5 and 10 Hz. North-component signal (the largest in amplitude in the swell and swell-harmonic bands) can be observed up to 130 km from the ice edge (Fig. B3, available in the supplemental material to this article). This energy is low signal-to-noise in the ice shelf interior, but is sufficiently coherent so that array analysis can be implemented with stacked signals. For successive 8 hr intervals, correlation lags were calculated using 75% overlapping one-minute time segments, using data from each of the 17 station pairs with a spatial separation of 20 km or less. Maximum correlation lags were measured for each of the (1400) station pair-specific time segment correlation functions, spanning each 8 hr data segment. The resulting discrete distribution

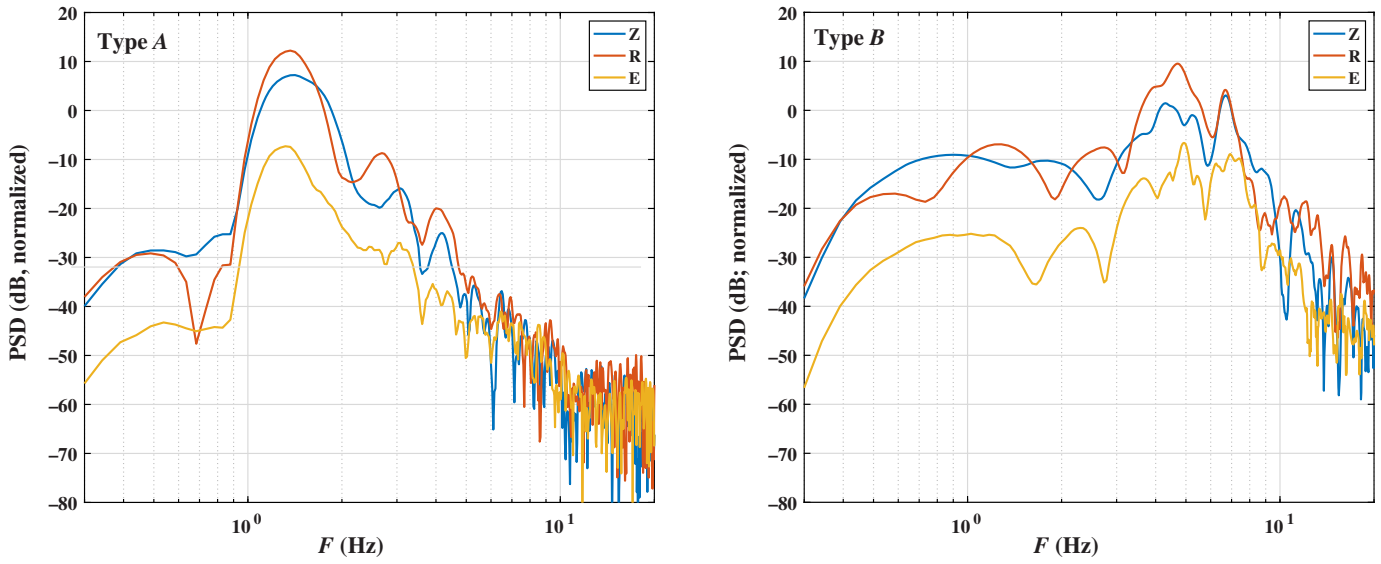

Figure 11. Normalized acceleration PSD for the high-pass filtered (>0.5 Hz) subevent stacks of Figure 9. The color version of this figure is available only in the electronic edition.

Downloaded from http://pubs.geoscienceworld.org/ssa/srl/article-pdf/doi/10.1785/0220200478/5285507/srl-2020478.1.pdf
by Bradley Lipovsky

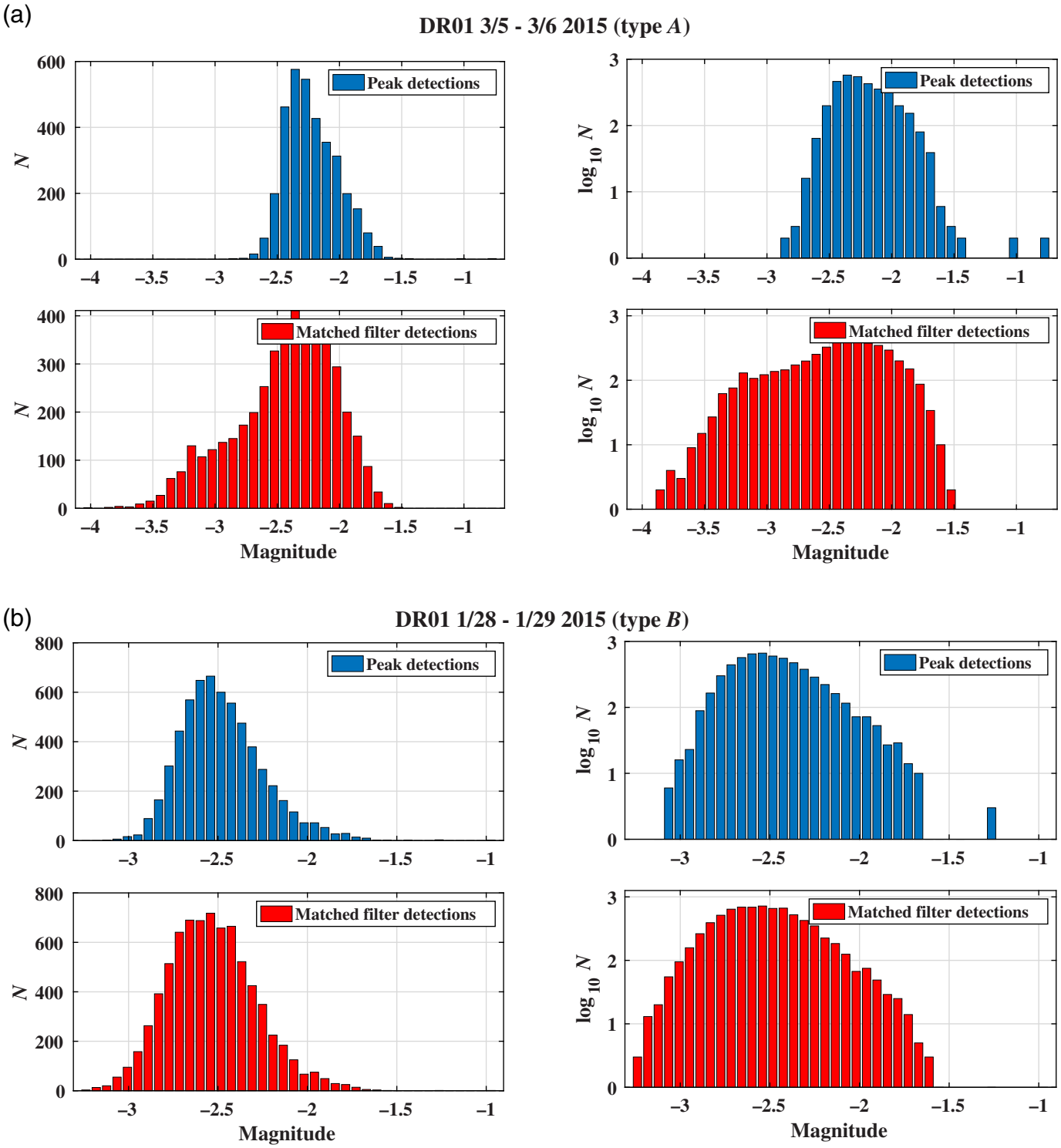

of correlation lags was then converted to a probability density function, using the Gaussian kernel method of Brandon (1996), and, a Gaussian function was subsequently fit to the principal probabilistic peak, to obtain a lag estimate and respective standard deviation. The best-fit (L_1 residual norm-minimizing) horizontally propagating plane wavefront was estimated using iteratively reweighted least-squares (e.g., Aster *et al.*, 2018). Correlation peaks, with energy-normalized

Figure 12. (a) Magnitude (2) distribution of type *A* subevents from 5 to 6 March 2015 (logarithmic and linear event counts; left and right, respectively). (b) Magnitude distributions for type *B* subevents from 28 to 29 2015. The color version of this figure is available only in the electronic edition.

Downloaded from http://pubs.geoscienceworld.org/ssa/srl/article-pdf/doi/10.1785/0220200478/5285507/srl-2020478.1.pdf
by Bradley Lipovsky

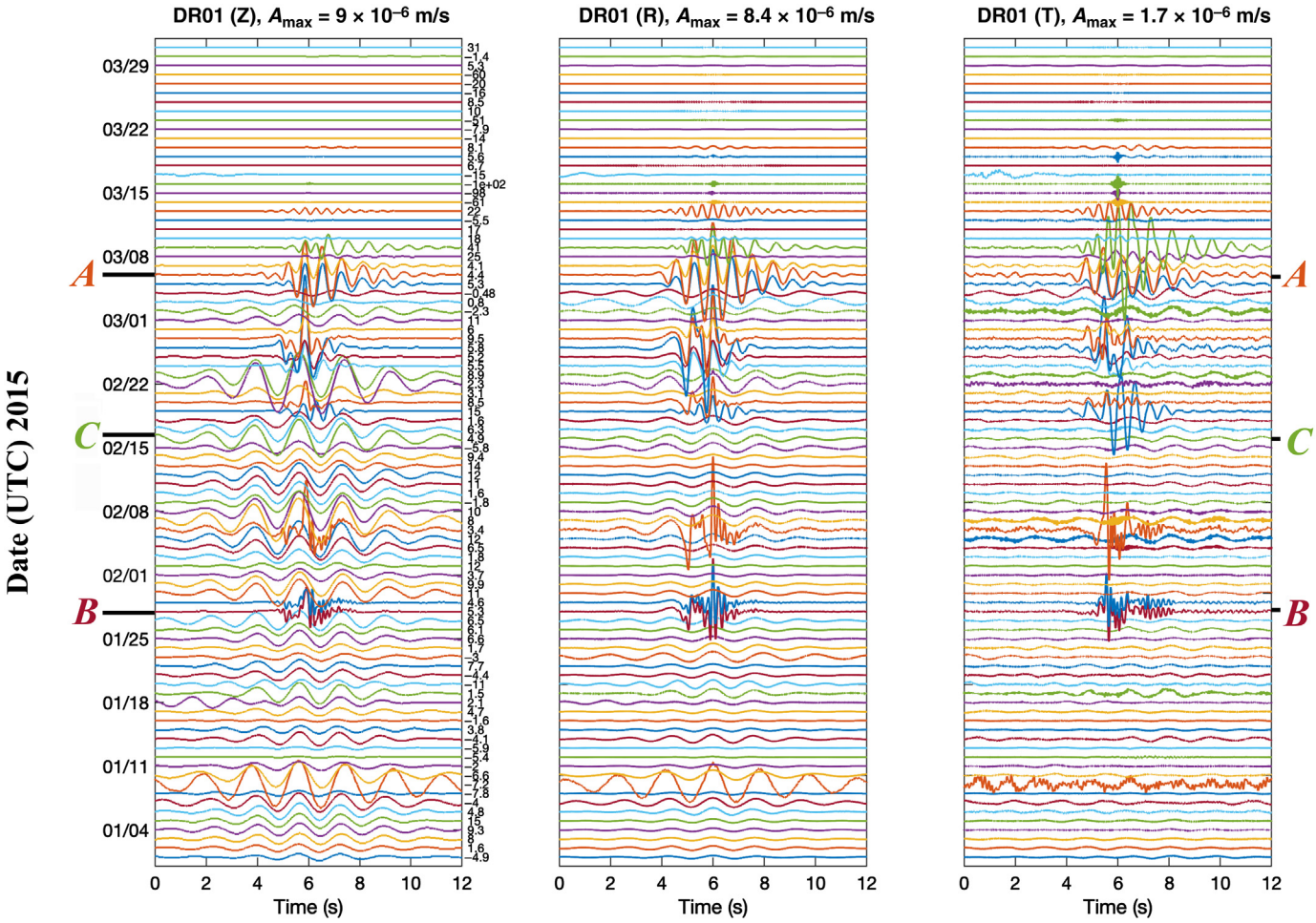

Figure 13. Characteristic 12 s three-component subevent seismograms at DR01 evaluated for daily UTC time periods between 1 January and 31 January 2015, calculated as robust true-amplitude stacks of matched filter detected events, with *A*, *B*, and *C* indicating representative event types, as described in the Time-domain observations section. Horizontal components (second two columns), are rotated via variance tensor diagonalization into R and T directions, to minimize T component energy. The orientation of the R component for each trace is noted (degree east of north) to the right of the Z-component subplot. In all cases, energy is strongly confined to a vertical plane. Orientations of all template events, for each day, are shown in Figure 15. Each group of component seismograms is scaled to its maximum amplitude component amplitude across all days (indicated in the respective titles). The color version of this figure is available only in the electronic edition.

peaks of less than 0.05 and/or standard deviations exceeding 5 s were removed as outliers. The resulting plane wavefront slowness vectors indicate near-front-normal propagation into the ice shelf interior and group velocities (99% confidence) between 3.50 and 2.53 km/s (Fig. 17 and Fig. B17, available in the supplemental material). This wave speed is consistent with fundamental-mode extensional Lamb waves, which are known to be commonly excited (e.g., by teleseismic shear waves coupling with the shelf near the grounding line; Baker *et al.*, 2020) and to propagate efficiently within the ice shelf, at a (nondispersive) velocity of, approximately, 3.2 km/s (e.g., Chen *et al.*, 2018; Lipovsky, 2018). The detection of a partially coherent Lamb wave signal, with approximately ice-front perpendicular propagation at this range, suggests that this intrashelf signal results from the superposition of a large number of small subevents in rough phase with each other over an appreciable extent of the near-shelf-front region.

Discussion

The observed near-front subevents (1) are statistically associated with swell conditions but are not strictly correlated with the short-term wave state of local wave activity (using the swell-band seismograms as a proxy for ocean wave state) at the ice shelf front, in either strict timing or magnitude (Fig. 18); (2) have short-term phase variability with respect to swell, as inferred from the long-period seismic signal observed near the ice edge (e.g., Fig. 5 and Fig. B5, available in the supplemental material); (3) are observed during low-swell episodes (e.g., Fig. 19), and are highly variable in number and size during high-swell episodes (Fig. 18); (4) exhibit

Downloaded from http://pubs.geoscienceworld.org/ssa/srl/article-pdf/doi/10.1785/0220200478/5285507/srl-2020478.1.pdf
by Bradley Lipovsky

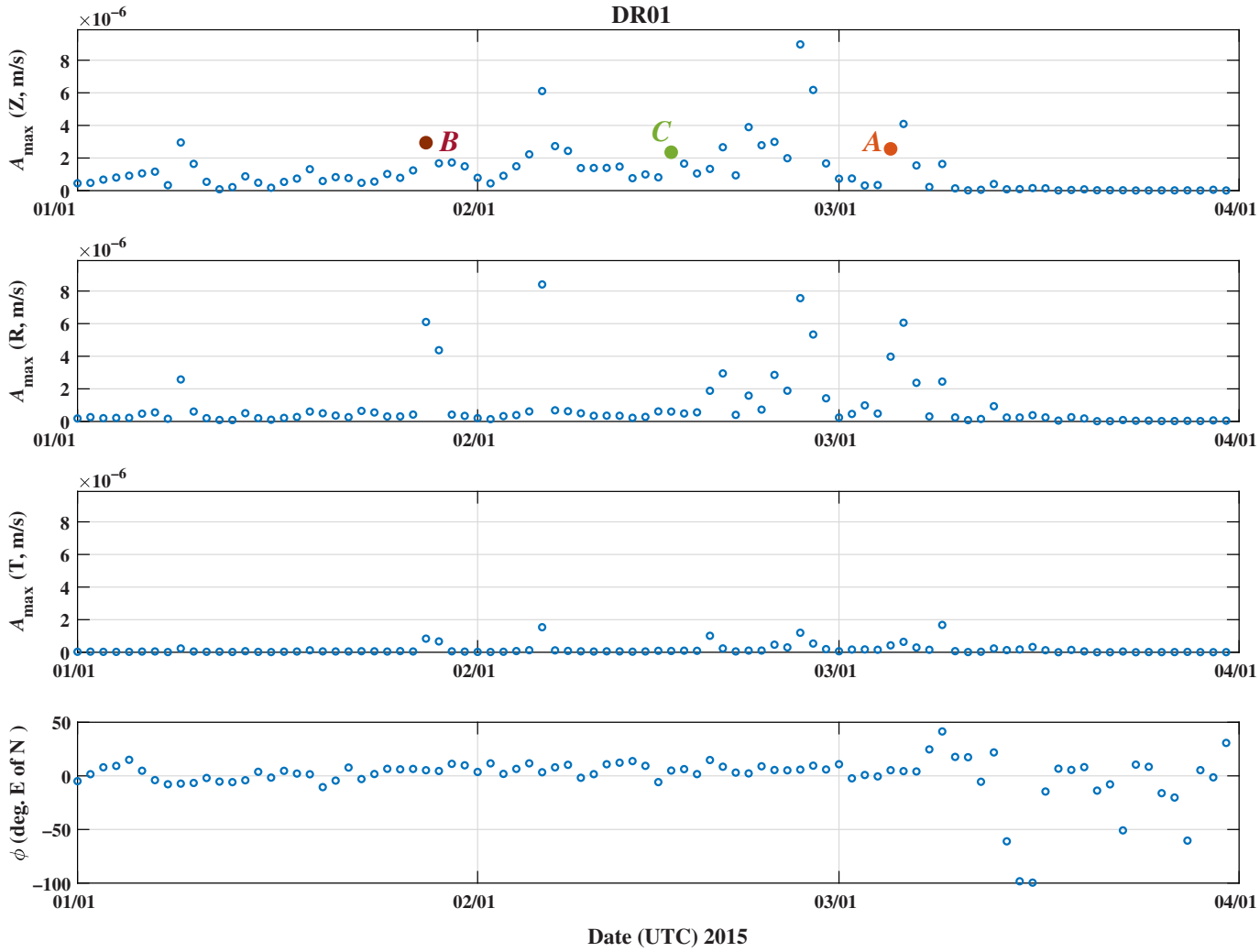

Figure 14. Amplitude and R-component particle motion azimuths (Fig. 13) for template daily stacks at DR01 between 1 January and 31 March 2015. Note the variable source azimuth, as constrained by the maximum R-component energy direction is toward the ice edge but also shows progressive variations with time. *A*, *B*, and *C* correspond to representative subevent types in Figure 13. Figures 15 and 16 depict corresponding daily subevent and swell-band horizontal polarization. The color version of this figure is available only in the electronic edition.

thresholding and hysteresis with respect to swell amplitude, and, show poor correlation with local swell amplitude, once becoming strongly excited (Fig. 8 and Fig. B10, available in the supplemental material). Each of these observations is difficult to reconcile with a seismic source that is directly due to the proportional action of ocean swell on the ice shelf (e.g., breaking and/or reflecting waves).

Subevent triggering threshold

The triggering threshold occurs at a swell energy metric (e) between, approximately, −85 and −75 dB (expressed as $20\log_{10}$ of the station-observed swell-band particle velocity amplitude in meters per second; Fig. 8 and Fig. B10, available in the supplemental material). These metrics correspond to swell-band seismic velocity amplitudes of $\approx 5.6\times10^{-5}$ to 1.8×10^{-4} m/s, respectively, or to seismic displacements of $\approx 1.3\times10^{-4}$ to 4.2×10^{-4} m at a characteristic swell period of 15 s (Fig. B4, available in the supplemental material). Using local ocean swell amplitude estimated from pressure observations 8 km from the ice front near DR01 by seafloor observatory station KPDR, which was deployed by the Korea Polar Research Institute between January and December 2015 (Fig. 1, Chen *et al.*, 2019) (Fig. 1) calculated an empirical amplitude transfer function T_{GSV} for vertical seismic displacement at DR01 with respect to ocean swell amplitude. T_{GSV} asymptotically approaches unity at very long periods, has a corner period $T_c \approx 60$ s, corresponding to periods near the flexural gravity wavelength (Lipovsky, 2018), and, falls off at ≈ -100 db/decade, at periods shorter than T_c (Fig. B18a, available in the supplemental material). Using a parametric approximation for the empirical T_{GSV} of Chen *et al.* (2019), extrapolated modestly to 0.1 Hz, we estimate

Downloaded from http://pubs.geoscienceworld.org/ssa/srl/article-pdf/doi/10.1785/0220200478/5285507/srl-2020478.1.pdf
by Bradley Lipovsky

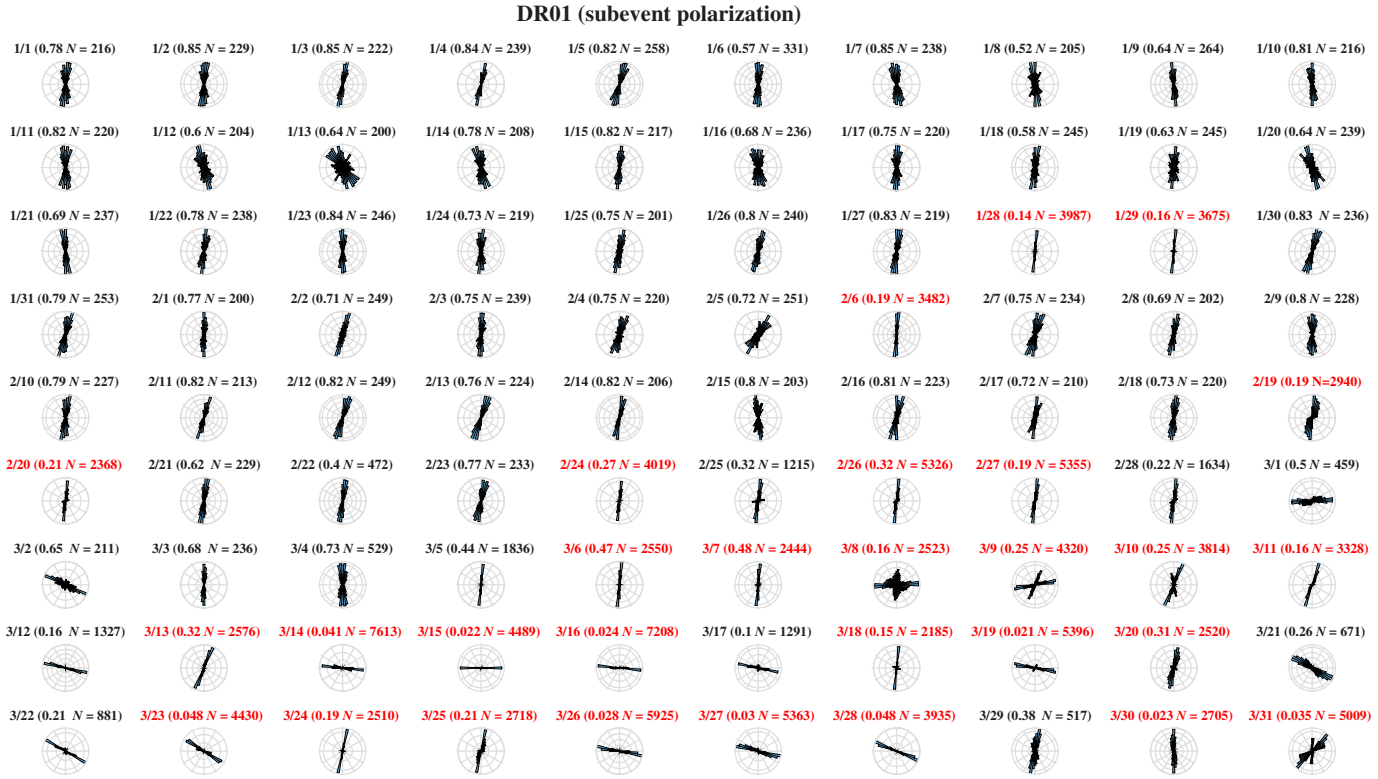

Figure 15. Rose horizontal-plane velocity polarization diagrams (north–up) of matched filter-detected subevents per day for 1 January–31 March 2015 (0.5–5 Hz filtering). Days with subevent numbers greater than 2000 are titled in red. Corresponding plots for DR02 and DR03 are shown in Figures B13 and B15 (available in the supplemental material), respectively. The color version of this figure is available only in the electronic edition.

$T_{GSV} \approx 1.1 \times 10^{-3}$ at 15 s period, for which a swell-period seismic displacement observed near the ice front of ≈1 mm corresponds to an ocean swell amplitude of, approximately, 0.9 m. The largest observed seismic swell-band amplitudes observed during 2015, at DR01 (during the exceptionally large episode on 1/28; Fig. 20), are, approximately, 8 mm, and, thus, would correspond to an ocean swell of, approximately, 7 m.

Ocean-strain coupling

The transfer function between ocean-wave amplitude (Chen *et al.*, 2019) is strongly peaked near T_c, which lies just below the swell period range and, thus, within the infragravity waveband (Fig. B18, available in the supplemental material) with typical spectral modes for swell and infragravity wave excitation near 15 and 80 s, respectively. Stress and strain arising from gravity-elastic wave flexure are strongly influenced by the persistent (e.g., Godin *et al.*, 2013) Southern Ocean infragravity wavefield. Pervasive infragravity wave excitation, at periods between 100 and 50 s, is only weakly attenuated (1–2 db) by winter sea ice and, thus, induces year-round ice shelf stress and strain in this period range. However, swell-band extremes in the summer (low sea ice) PSD amplitude spectrum can exceed those of the infragravity waveband by, up to, approximately, 30 dB at RIS ice front stations. Swell excitation of the near-front ice shelf is reduced by 15–20 dB, during austral winter due to sea ice attenuation (Baker *et al.*, 2019).

We estimate the magnitude of swell-induced ice shelf gravity-elastic wave elastic stresses and strains, using the model of Lipovsky (2018). The linear transfer function between vertical seismic velocity and extensional stress (the flexural wave impedance) shows a maximum at periods near T_c but falls off only weakly (approximately, 20%) in amplitude between its maximum and 10 s period. This allows for the highest intervals of ice shelf ocean-induced stress and strain to be dominated by the influence of swell during the relatively sea ice-free period between, approximately, December and March (Baker *et al.*, 2019). For the ice geometry near the DR01-03 stations, where subevents are observed (Fig. B18, available in the supplemental material), the swell band range between 0.03 and 0.12 Hz corresponds to a flexural wave impedance in the range of 17–25 KPa/(mm/s). Observed DR01 threshold seismic velocity amplitudes of $\approx 5.6 \times 10^{-5}$ to 1.8×10^{-4} m/s, at periods near 15 s, thus, correspond to flexural stresses and strains near the shelf surface or base of ≈1.2 to 3.8 KPa and 1.3×10^{-7} to 4.3×10^{-7}, respectively. This triggering strain range is comparable to that estimated for dynamic icequake (Peng *et al.*, 2014) as well as in teleseismic surface-wave

Downloaded from http://pubs.geoscienceworld.org/ssa/srl/article-pdf/doi/10.1785/0220200478/5285507/srl-2020478.1.pdf
by Bradley Lipovsky

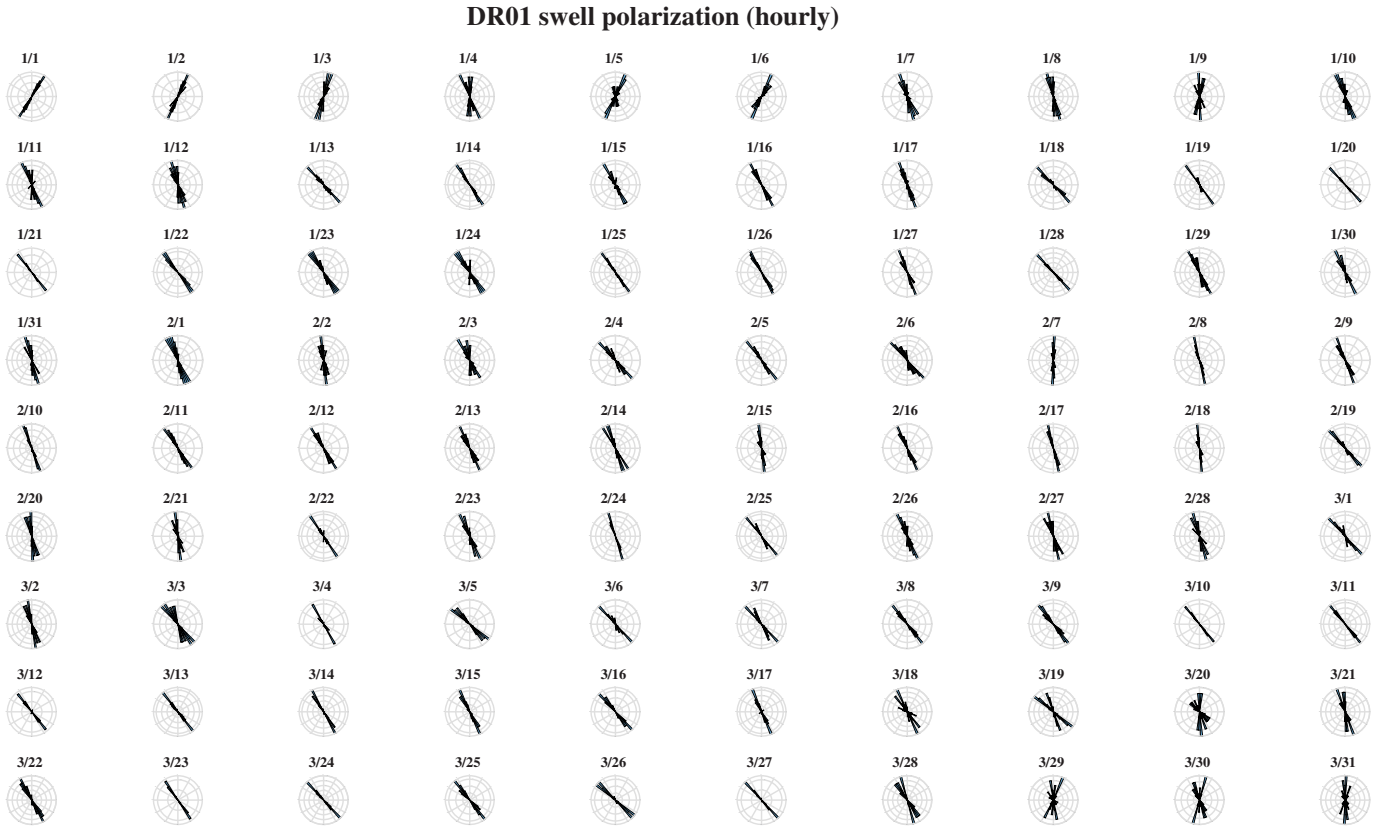

Figure 16. Rose horizontal-plane velocity polarization diagrams (north–up) of swell-band velocity in hourly bins for UTC days 1 January–31 March 2015 (0.03–0.12 Hz filtering). Corresponding plots for DR02 and DR03 are shown in Figures B14 and B16 (available in the supplemental material), respectively. The color version of this figure is available only in the electronic edition.

microearthquake triggering studies (e.g., Brodsky and van der Elst, 2014), in which triggering is observed at dynamic peak strains as low as a few times 10^{-9}.

We calculate wave stresses and strains using vertical-component seismograms from DR01 and relevant ice shelf and ocean parameters, using the corresponding transfer function shown in (Fig. B18b, available in the supplemental material), which also enables us to create stress and strain spectrograms (Fig. 21) that can be integrated across frequency bands of particular interest. Maximum dynamic stress and strain occurs in the swell band, but this excitation only occurs sporadically during the largest swell episodes. The near-continuous perturbation of the ice shelf integrated across in the infragravity waveband is commonly at or just below the lower threshold for subevent triggering. This is generally consistent with the conclusion of Chen *et al.* (2019), who noted that infragravity wave excitation may precondition the shelf for near-edge seismogenic fracture, as represented by the larger magnitude event population.

Source mechanisms

A more detailed fracture seismic source analysis is beyond the scope of this observational study. However, some immediate comments can be emphasized here. Two principal hypotheses present themselves. The first, and, perhaps, the simplest, is that we are observing the direct effect of ice cliff-ocean swell impacts and a stimulated resonant (particularly, in the case of the more narrowband types *A* and *C* signals) response at the ice edge (e.g., Zhuchkova and Kouzov, 2012). However, on closer examination, we note several aspects of the triggered events that are inconsistent with a simple direct wave impact seismic source that responds uniformly to swell state. Specifically, we note (1) hysteresis in the time evolution of swell versus high-frequency radiation (e.g., Fig. 8 and Fig. B10, available in the supplemental material), including a delayed onset and trailing persistence in subevent occurrence across distinct swell episodes, as well as a poor correlation between subevent and swell energy during strong excitation; (2) swell and stress–strain threshold behavior for the most pronounced subevent excitation intervals, visible in hysteresis plots (Fig. 8 and Fig. B10, available in the supplemental material), subevent times (Fig. 20), and spectrogram-observed delayed onsets of harmonic spectral features (e.g., Fig. 3); and (3) the sporadic occurrence of subevents during low swell and subthreshold conditions

Downloaded from http://pubs.geoscienceworld.org/ssa/srl/article-pdf/doi/10.1785/0220200478/5285507/srl-2020478.1.pdf
by Bradley Lipovsky

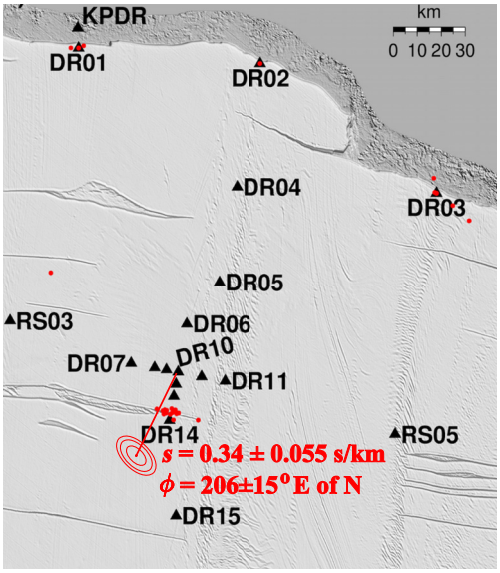

Figure 17. Stacked array processing in the 0.5–5 Hz frequency band at the DR10 array spanning the first four hours of 6 March 2015 (e.g., Fig. 4), as described in the section Intrashelf seismic illumination by high-frequency swell-triggered energy. Error ellipses indicate 68%, 95%, and 99% slowness vector error ellipsoids obtained from the L_1-minimizing best-fit covariance matrix (p-value of 0.86; see Fig. B17, available in the supplemental material). Background figure shows ice shelf morphology and source location estimates for large ice front and rift events (red dots) after Chen *et al.* (2019). Background Moderate Resolution Imaging Spectroradiometer (MODIS) ice shelf morphology from Scambos *et al.* (2007). The color version of this figure is available only in the electronic edition.

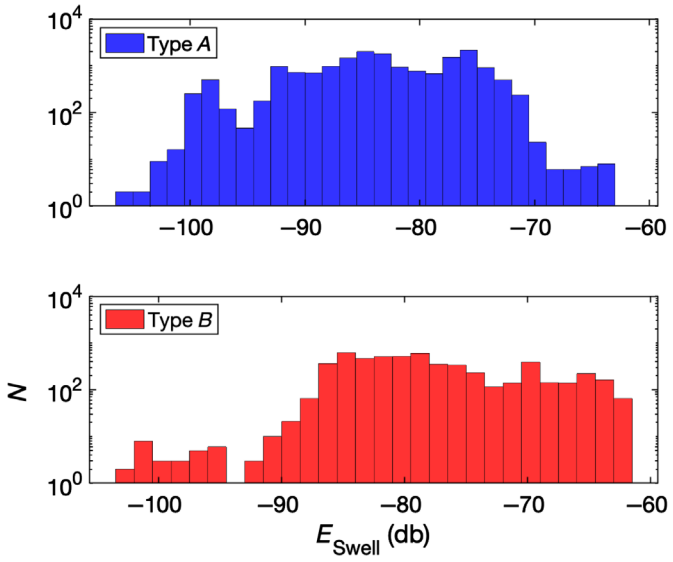

Figure 18. Swell energy levels during the occurrence of the two impulsive event types (Fig. 20) in logarithmic count scale histograms. Note the occurrence of both event types during a wide range of swell energy levels. The color version of this figure is available only in the electronic edition.

(Fig. 20). These observations demonstrate a nonlinear and statistical, as opposed to a deterministic, association between subevent occurrence and the concurrent swell amplitude or phase.

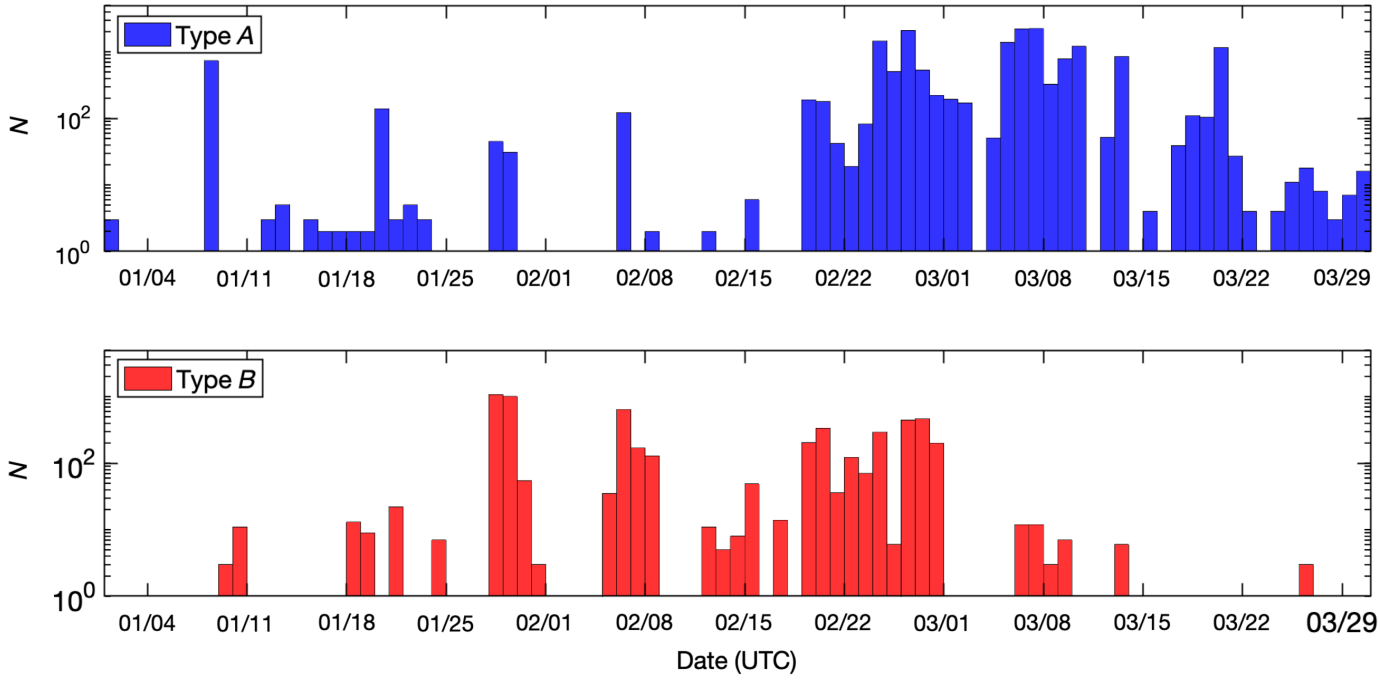

Figure 19. Histograms (logarithmic count scale) of event numbers for the two impulsive event types corresponding to Figs. 18 and 20. The color version of this figure is available only in the electronic edition.

Downloaded from http://pubs.geoscienceworld.org/ssa/srl/article-pdf/doi/10.1785/0220200478/5285507/srl-2020478.1.pdf
by Bradley Lipovsky

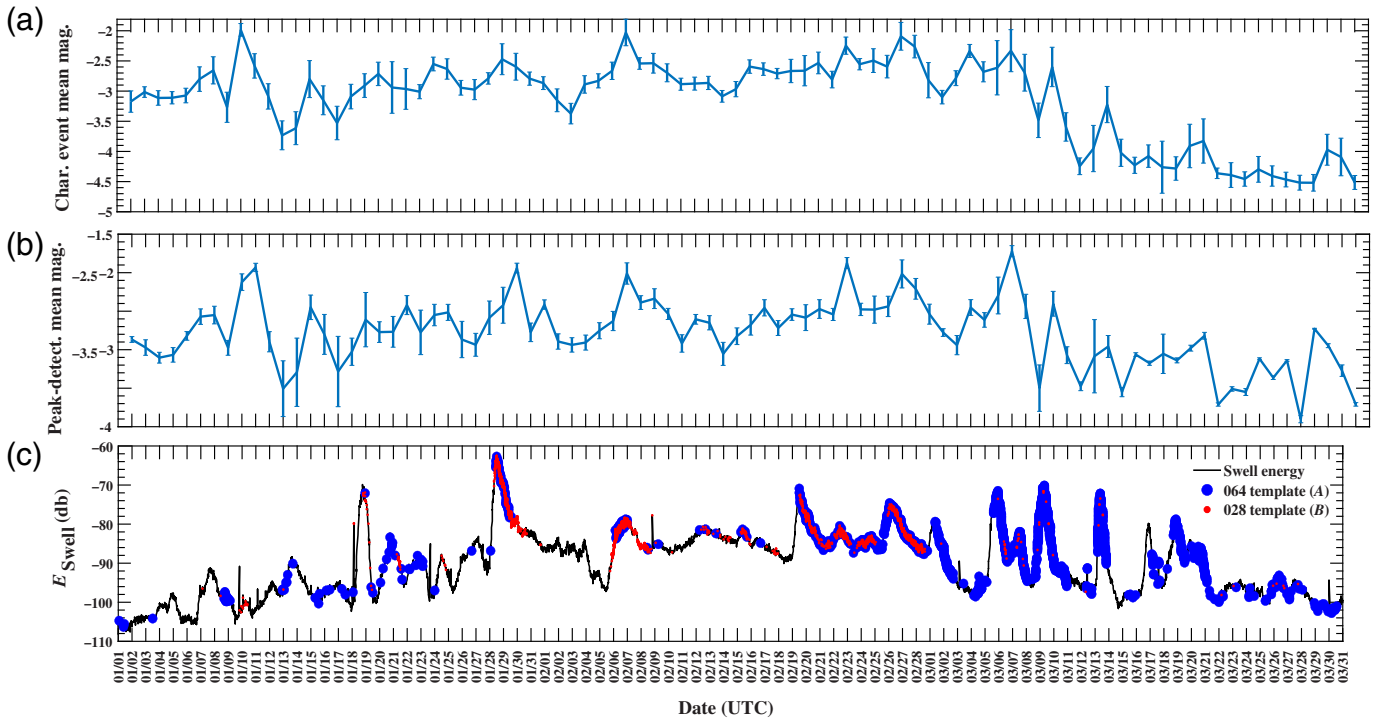

Figure 20. (a) Daily mean characteristic and (b) peak-detected event magnitudes and associated standard deviations calculated using equation (2) at DR01 between 1 January and 31 March 2015. (c) Corresponding subevent detections for characteristic impulsive template waveforms using robust stacks extracted from the highly active days 6 March (type *A*) and 28 January (type *B*) (Fig. 13) extracted using moving window correlation detection of the north seismogram component and a cross-correlation coefficient threshold of 0.5. Swell energy is quantified using the velocity amplitude squared between 0.03 and 0.12 Hz, convolved with a 1 hr area-normalized Bartlett. Corresponding daily subevent counts are shown in Figure 19. The color version of this figure is available only in the electronic edition.

Fracture propagation, at a threshold stress level, is a basic feature of linear elastic fracture mechanics (Van der Veen, 1998), and we can crudely estimate the source dimensions that would be needed to generate the observed subevent waveforms. Because of our sparse station observations, these basic calculations are insensitive to total fracture length L, the sense of motion (e.g., opening vs. shearing), and source depth. We find that the observations are able to constrain consistent sources mechanisms to one of two nonexclusive scenarios. We note that these events must represent small displacements. An event with a magnitude of −2 (e.g., Fig. 12) corresponds to a seismic moment of, approximately, $M_0 = 1.3 \times 10^6$ N · m (e.g., Hanks and Kanamori, 1979). Using $M_0 = \mu A d$, in which μ is the rigidity, A is the source area, and d is a displacement, a faulting source with a radiating area of 100 m^2 and $\mu = 8.7 \times 10^9$ Pa (Fig. B18, available in the supplemental material) would require an event of this size to correspond to a displacement of around 1.5 μm and a seismic potency, $Ad \approx 1.5 \times 10^{-4}$ m^3. Of course, this particular source dimension of 100 m^2 is entirely conjectural and scales inversely with d, but is, at least, plausible, given the scale of the block-delineating fractures observed near the ice edge with map view extents of up to several 100s of meters. Visual imagery, additionally, would not reveal possible obscured seismogenic fractures, such as fully bridged crevasses or basal crevasses (Lipovsky and Dunham, 2015). In this simple conceptualization, type *B* events may represent either higher frequency modes of excitation in fracture systems or brittle fracture expansion occurring during periods of large swell-induced excitation, such as the exceptional 28–29 January *B*-type dominated swell event (Figs. 18 and 21). Interestingly, type *B* events cease near the end of the sea-ice free period (early March) at DR01. This may represent a change in near-front fracture configuration, precipitated by ice loss and/or a change in the fatigue state of a near-front damage zone.

Worldview imagery of the ice front region, with resolution approaching 0.5 m during the network deployment near DR01 (Fig. 22), and DR02 and DR03 (Figs. B19 and B20, available in the supplemental material), indicates near-front features that are candidates for repeating seismic source zones under the influence of swell-induced oscillatory stress and stain. We also note visual evidence, in the form of melange zones and recently calved blocks, of recent small-scale ice-front failures along such features. We hypothesize that seismic subevents are excited via persistent oscillatory stressing of these structures within the near-front damage zone, where the presence of the ice edge

Downloaded from http://pubs.geoscienceworld.org/ssa/srl/article-pdf/doi/10.1785/0220200478/5285507/srl-2020478.1.pdf
by Bradley Lipovsky

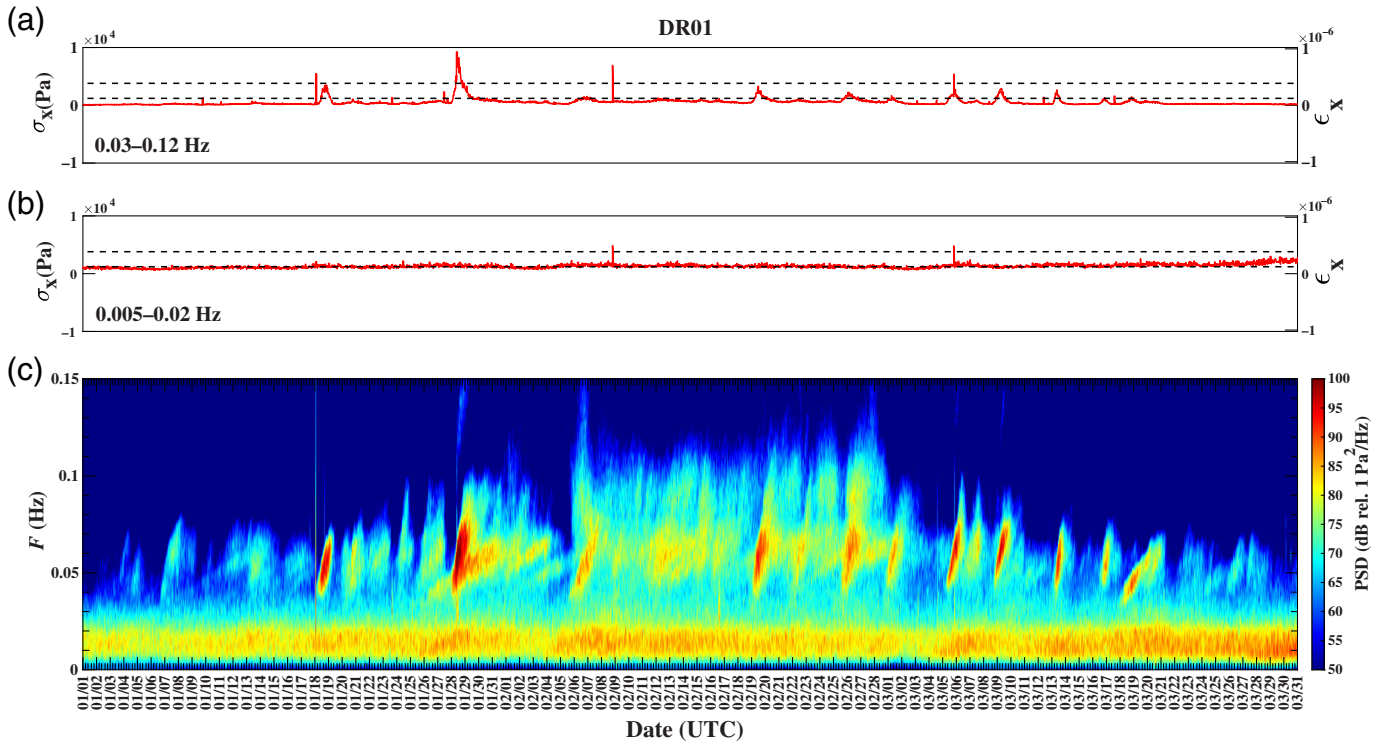

Figure 21. Extensional stress and strain (1 hr maximal moving window) levels in the swell (a) 0.03–0.12 Hz and infragravity (b) 0.005–0.02 Hz bands, using a value of Young's modulus of $E = 8.7 \times 10^9$ Pa, at DR01 1 January–31 March 2015 (compare to Fig. 2). Black dashed lines (1.2, 3.8 KPa) correspond to the observed threshold subevent triggering levels discussed in the section Ocean-strain coupling. (c) Associated stress PSD spectrogram that demonstrates the predomince of the swell-band stress and strain perturbation during prominent swell events. Spike-like transients reflect signals from icequakes and earthquakes. The color version of this figure is available only in the electronic edition.

and its perturbation by ocean gravity-elastic waves produces evolving fractures. In this conceptualization (Fig. 23), fracture-generated source zones become strongly and repeatedly seismogenic at stress and strain levels above the observed swell-induced stress–strain threshold (Fig. 21). Of particular note in the satellite imagery are arcuate front parallel fractures near the ice edge that may be both seismogenic and delineate incipient failure margins. The gravitational collapse of such fractures may be responsible for seismic events in the distinct larger magnitude population, some of which may also generate local ocean gravity wave events (MacAyeal *et al.*, 2009; Fig. 6). Haran *et al.* (2018) suggests that such an ongoing front-wasting process may result in, approximately, 7–23 m/yr of average front loss at the Ross, consistent with the early observations of Crary and Chapman (1963). This ongoing smaller-scale wasting complements sporadic larger-scale front step-backs due to the calving of tabular icebergs (e.g., Lazzara *et al.*, 2008; Martin *et al.*, 2010).

Conclusions

The gravity-elastic excitation of the RIS by ocean swell triggers small, near-front high-frequency (relative to swell) seismic signals that occur at rates of up to thousands per hour. During some swell events, the timing of these subevents becomes sufficiently phase synchronized with the incoming swell that strong swell integer multiple harmonics appear in spectra and spectrograms calculated for time windows that span many swell cycles. This spectral phenomenon arises due to a Dirac comb process that we mathematically describe and numerically simulate in the Appendix. We identify three categories of subevents, all excited near the ice edge, based on their seismic waveforms. All subevent types generate Rayleigh-wave-type elliptical particle motions that are consistent with predominantly southward propagation into the ice shelf interior. The gravity-elastic swell-band flexural excitation of the ice shelf is estimated to produce near-front extensional stresses and strains that exceed several kilopascal and tens to hundreds of nanostrain, respectively. These stress and strain levels are comparable or exceed those attributed in other settings to Rayleigh-wave triggering of earthquake and icequake seismicity, in similar excitatory period bands. The prolific swell-triggered subevents exhibit unusually low-frequency content (between, approximately, 1 and 10 Hz) for events of such small size, with local magnitudes estimated to be $\lesssim -1.5$. A small population of significantly larger events may be associated with ice front calving events that have previously been statistically correlated with swell perturbation of the ice front region (Chen *et al.*, 2019). We observe the seismic wavefield

Downloaded from http://pubs.geoscienceworld.org/ssa/srl/article-pdf/doi/10.1785/0220200478/5285507/srl-2020478.1.pdf
by Bradley Lipovsky

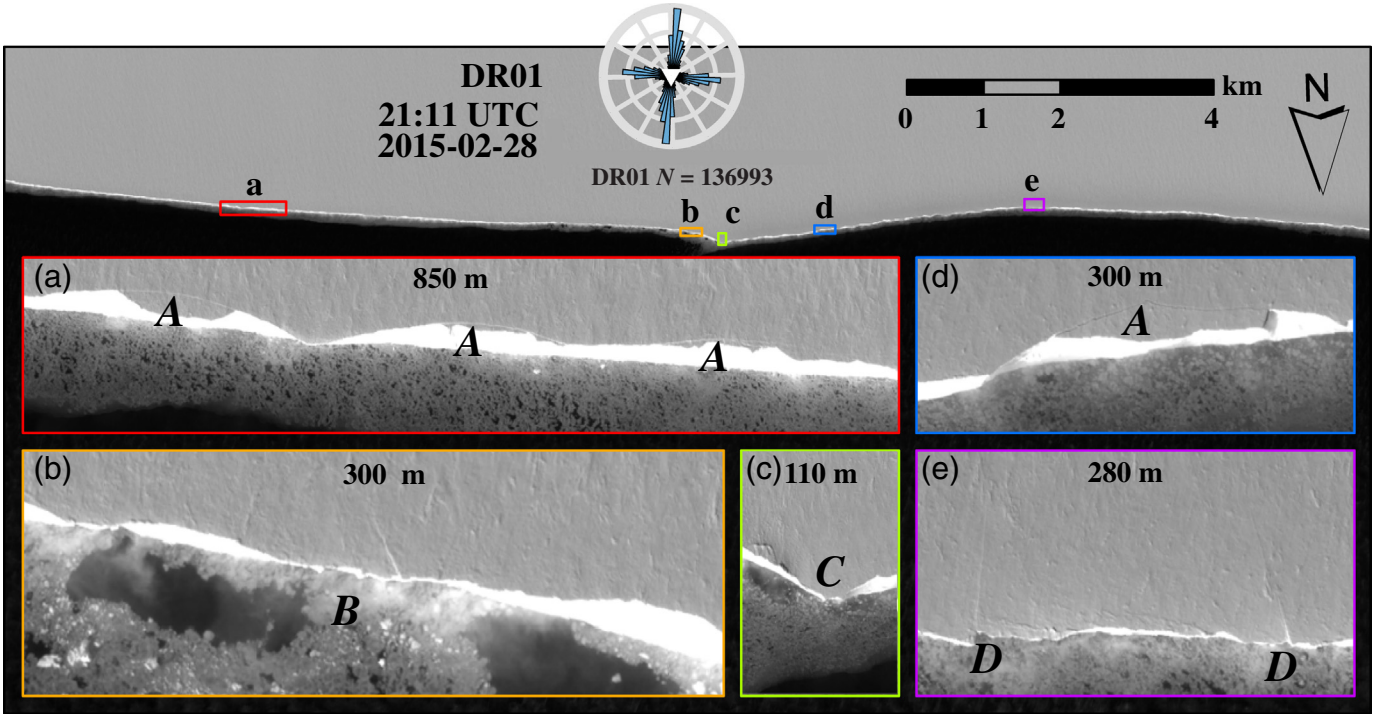

Figure 22. Worldview imagery (2015, 2016, DigitalGlobe, Inc.) of the ice front near DR01 on 28 February 2015, with inset images identified (a–e, with east–west respective distances indicated). Structures of potential seismogenic interest include incipient iceberg blocks bounded by arcuate surface-terminating crevasses (A), fragmented shelf ice from recent calving or spalling (B), anomalous high-curvature ice front geometry (C), and front-perpendicular fractures extending to the ice edge (D). Similar imagery near-stations DR02 and DR03 show that these features are pervasive along the central RIS (Figs. B19 and B20, available in the supplemental material). Cumulative rose polarization diagram (from the daily 1 January to 31 March 2015 diagrams of Fig. 15) is shown at the station location. The color version of this figure is available only in the electronic edition.

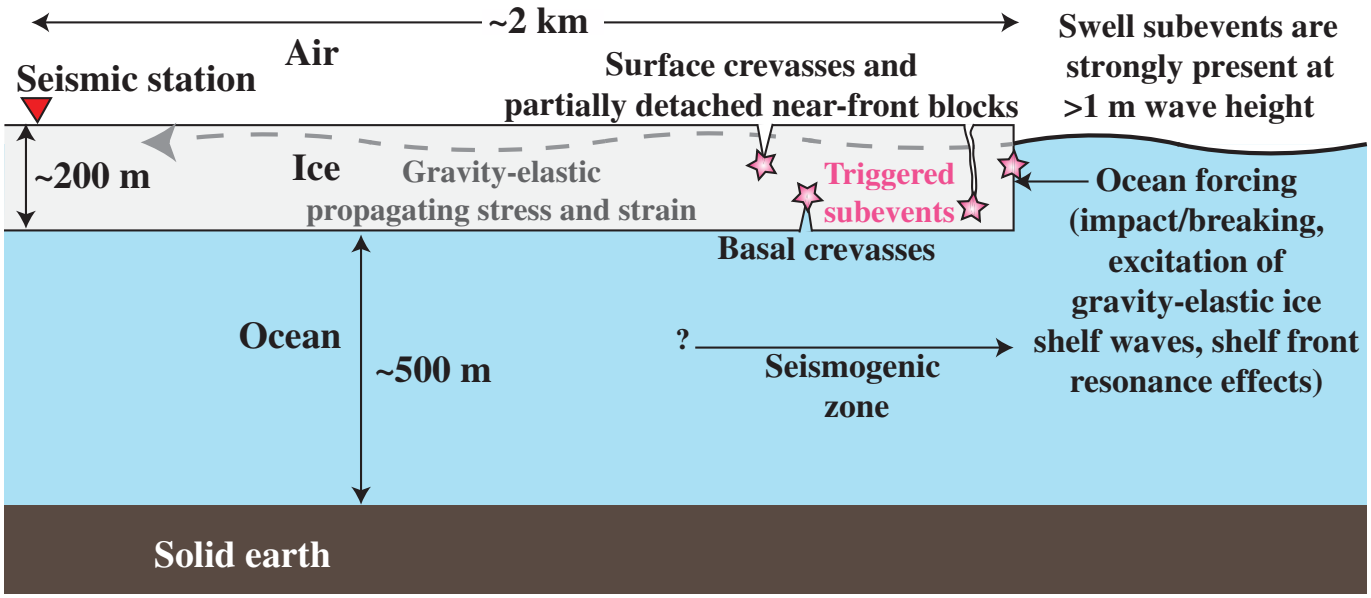

Figure 23. Conceptual depiction of hypothesized seismogenic and associated processes in the ice shelf front region (vertical–horizontal scale preserved), interpreted from Figure 1B. The color version of this figure is available only in the electronic edition.

Downloaded from http://pubs.geoscienceworld.org/ssa/srl/article-pdf/doi/10.1785/0220200478/5285507/srl-2020478.1.pdf
by Bradley Lipovsky

generated by this activity at near-front seismic stations separated by, approximately, 100 km and, more weakly, at stations on the shelf interior that are located up to more than 100 km from the front. This widespread, high-frequency ($\gtrsim$1 Hz) extensional Lamb guided wavefield may, thus, provide opportunities for the imaging and time-lapse monitoring of ice shelves.

Subevent occurrence during swell episodes exhibits triggering and hysteresis behavior characterized by delayed onset and prolonged decay (of up to several hours) relative to the swell excitation energy. Subevents are also observed during low-swell excitation, suggesting a background seismic process that becomes strongly enhanced when gravity-elastic stressing in the swell band exceeds, approximately, 1.2–3.8 KPa. We propose that these events represent the activity of triggered intra-shelf subevent mechanism(s) occurring within a damage zone that encompasses the first few hundred meters of the ice front region, where satellite imagery reveals possible seismogenic features. Denser seismic and multidisciplinary observations at the ice front may be necessary to definitively test these source hypotheses, and to clarify the influences of direct wave impacts, evolving front geometry (e.g., Wagner *et al.*, 2014) and swell directivity (Cathles *et al.*, 2009; Hell *et al.*, 2019, 2020).

Data and Resources

Seismic data from 2014 to 2017, used in this study, are available through the Incorporated Research Institutions for Seismology Data Management Center (IRIS-DMC) under Ross Ice Shelf (RIS) and DRIS network code XH. The seismic instruments were provided by the IRIS through the Program for the Array Seismic Studies of the Continental Lithosphere (PASSCAL) Instrument Center at New Mexico Tech. Regional maps were generated with the Generic Mapping Tools (GMT, Wessel and Smith, 1998). Geospatial support for this work provided by the Polar Geospatial Center under National Science Foundation Office of Polar Programs (NSF-OPP) Award Numbers 1043681 and 1559691. Worldview Imagery 2015, 2016 DigitalGlobe, Inc. The supplemental materials include 20 additional figures relevant to swell-triggered subevents on the RIS (Appendix B) and MATLAB code www.mathworks.com/products/matlab, last accessed March 2020; version 9.9.0.1467703 (R2020b) that replicates the Dirac comb numerical modeling figures in Appendix B (Appendix C).

Conflicts of Interest

The authors acknowledge that there are no conflicts of interest recorded.

Acknowledgments

This research was supported by the National Science Foundation (NSF) Grant Numbers PLR-1142518, 1141916, 1142126, 1246151, 1246416, and 1853896. Peter D. Bromirski also received support from the California Department of Parks and Recreation, Division of Boating and Waterways, under Contract Number 11-106-107. The authors thank Reinhard Flick and Patrick Shore for their support during field work, Tom Bolmer in preparing maps, and the U.S. Antarctic Program for logistical support. The facilities of the Incorporated Research Institutions for Seismology (IRIS) Consortium are supported by the National Science Foundation (NSF) under Cooperative Agreement EAR-1261681 and the U.S. Department of Energy (DOE) National Nuclear Security Administration.

References

Anthony, R., R. Aster, D. Wiens, S. Anandakrishan, A. D. Huerta, J. P. Winberry, T. Wilson, and C. Rowe (2015). The seismic noise environment of Antarctica, *Seismol. Res. Lett.* **86,** 89–100, doi: 10.1785/0220140109.

Aster, R., and J. P. Winberry (2017). Glacial seismology, *Rep. Progr. Phys.* **80,** 126801, doi: 10.1088/1361-6633/aa8473.

Aster, R., D. McNamara, and P. Bromirski (2010). Global trends in extremal microseism intensity, *Geophys. Res. Lett.* **37,** L14303, doi: 10.1029/2010gl043472.

Aster, R., C. Thurber, and B. Borchers (2018). *Parameter Estimation and Inverse Problems*, Third Ed., Elsevier, 404, available at https://books.google.com/books?id=LXgSA6YEke4C (last accessed January 2021).

Baker, M., R. Aster, R. Anthony, J. Chaput, D. Wiens, A. Nyblade, P. D. Bromirski, P. Gerstoft, R. A. Stephen, and P. Gerstoft (2019). Seasonal and spatial variations in the ocean-coupled ambient wavefield of the Ross Ice Shelf, *J. Glaciol.* **65,** 1–14.

Baker, M., R. C. Aster, D. A. Wiens, A. Nyblade, P. D. Bromirski, P. Gerstoft, and R. A. Stephen (2020). Teleseismic earthquake wavefields observed on the Ross Ice Shelf, *J. Glaciol.* 1–17, doi: 10.1017/jog.2020.83.

Banwell, A. F., I. C. Willis, G. J. Macdonald, B. Goodsell, and D. R. MacAyeal (2019). Direct measurements of ice-shelf flexure caused by surface meltwater ponding and drainage, *Nat. Comm.* **10,** no. 1, 730, doi: 10.1038/s41467-019-08522-5.

Banwell, A. F., I. C. Willis, G. J. Macdonald, B. Goodsell, D. P. Mayer, A. Powell, and D. R. Macayeal (2017). Calving and rifting on the McMurdo Ice Shelf, Antarctica, *Ann. Glaciol.* **58,** 78–87, doi: 10.1017/aog.2017.12.

Barletta, V. R., M. Bevis, B. E. Smith, T. Wilson, A. Brown, A. Bordoni, M. Willis, S. A. Khan, M. Rovira-Navarro, I. Dalziel, *et al.* (2018). Observed rapid bedrock uplift in Amundsen Sea Embayment promotes ice-sheet stability, *Science* **360,** no. 6395, 1335.

Bartholomaus, T., J. Amundson, J. Walter, S. O'Neel, M. West, and C. Larsen (2015). Subglacial discharge at tidewater glaciers revealed by seismic tremor, *Geophys. Res. Lett.* **42,** 6391–6398, doi: 10.1002/2015GL064590.

Bassis, J. N., H. A. Fricker, R. Coleman, and B. Minster (2008). An investigation into the forces that drive ice-shelf rift propagation on the Amery Ice Shelf, east Antarctica, *J. Glaciol.* **54,** no. 184, 17–27.

Bracewell, R. N. (1986). *The Fourier Transform and its Applications*, Vol. 31,999, McGraw-Hill, New York, New York.

Brandon, M. T. (1996). Probability density plot for fission-track grain-age samples, *Radiat. Meas.* **26,** no. 5, 663–676.

Brodsky, E. E., and N. van der Elst (2014). The uses of dynamic earthquake triggering, *Ann. Rev. Earth Planet. Sci.* **42,** 317–339, doi: 10.1146/annurev-earth-060313-054648.

Bromirski, P. D., Z. Chen, R. A. Stephen, P. Gerstoft, D. Arcas, A. Diez, R. C. Aster, D. A. Wiens, and A. Nyblade (2017). Tsunami and infragravity waves impacting Antarctic ice shelves, *J. Geophys. Res.* **122,** no. 7, 5786–5801, doi: 10.1002/2017JC012913.

Downloaded from http://pubs.geoscienceworld.org/ssa/srl/article-pdf/doi/10.1785/0220200478/5285507/srl-2020478.1.pdf
by Bradley Lipovsky

Bromirski, P. D., A. Diez, P. Gerstoft, R. A. Stephen, T. Bolmer, D. Wiens, R. C. Aster, and A. Nyblade (2015). Ross ice shelf vibrations, *Geophys. Res. Lett.* **42,** 75897597, doi: 10.1002/2015GL065284.

Bromirski, P. D., O. V. Sergienko, and D. R. MacAyeal (2010). Transoceanic infragravity waves impacting Antarctic ice shelves, *Geophys. Res. Lett.* **37,** doi: 10.1029/2009gl041488.

Brunt, K. M., E. Okal, and D. MacAyeal (2011). Antarctic ice-shelf calving triggered by the Honshu (Japan) earthquake and tsunami, March 2011, *J. Glaciol.* **57,** no. 205, 785–788.

Cathles, L. M., E. A. Okal, and D. R. Mac Ayeal (2009). Seismic observations of sea swell on the floating Ross Ice Shelf, Antarctica, *J. Geophys. Res.* **114,** doi: 10.1029/2007JF000934.

Chaput, J., R. C. Aster, D. McGrath, M. Baker, R. E. Anthony, P. Gerstoft, P. Bromirski, A. Nyblade, R. A. Stephen, D. A. Wiens, *et al.* (2018). Near-surface environmentally forced changes in the Ross Ice Shelf observed with ambient seismic noise, *Geophys. Res. Lett.* **45,** no. 20, 11,187–11,196, doi: 10.1029/2018gl079665.

Chen, Z., P. D. Bromirski, P. Gerstoft, R. A. Stephen, W. S. Lee, S. Yun, S. D. Olinger, R. C. Aster, D. A. Wiens, and A. A. Nyblade (2019). Ross Ice Shelf icequakes associated with ocean gravity wave activity, *Geophys. Res. Lett.* doi: 10.1029/2019GL084123.

Chen, Z., P. D. Bromirski, P. Gerstoft, R. A. Stephen, D. A. Wiens, R. C. Aster, and A. A. Nyblade (2018). Ocean-excited plate waves in the Ross and Pine Island Glacier Ice Shelves, *J. Glaciol.* 1–15, doi: 10.1017/jog.2018.66.

Crary, A. P., and W. H. Chapman (1963). Additional glaciological measurements at the abandoned Little America Station, Antarctica, *J. Geophys. Res.* **68,** no. 21, 6064–6065, doi: 10.1029/JZ068i021p06064.

Das, I., L. Padman, R. E. Bell, H. A. Fricker, K. J. Tinto, C. L. Hulbe, C. S. Siddoway, T. Dhakal, N. P. Frearson, C. Mosbeux, *et al.* (2020). Multidecadal basal melt rates and structure of the Ross Ice Shelf, Antarctica, using airborne ice penetrating radar, *J. Geophys. Res.* **125,** no. 3, doi: 10.1029/2019jf005241.

Diez, A., P. D. Bromirski, P. Gerstoft, R. A. Stephen, R. Anthony, R. Aster, C. Cai, A. Nyblade, and D. A. Wiens (2016). Ice shelf structure derived from dispersion curve analysis of ambient seismic noise, Ross Ice Shelf, Antarctica, *Geophys. J. Int.* **205,** 785–795.

Fretwell, P., H. D. Pritchard, D. G. Vaughan, J. L. Bamber, N. E. Barrand, R. Bell, C. Bianchi, R. G. Bingham, D. D. Blankenship, G. Casassa, *et al.* (2013). Bedmap improved ice bed, surface and thickness datasets for Antarctica, *Cryosphere* **7,** no. 1, 375–393.

Furst, J., G. Durand, G. Gillet-Chaulet, L. Tavard, M. Rankl, M. Braun, and O. Gagliardini (2016). The safety band of Antarctic ice shelves, *Nat. Clim. Change* doi: 10.1038/nclimate2912.

Glasser, N., and T. Scambos (2008). A structural glaciological analysis of the 2002 Larsen B Ice shelf collapse, *J. Glaciol.* **54,** no. 184, 3–16.

Godin, O. A., and N. Zabotin (2016). Resonance vibrations of the Ross Ice Shelf and observations of persistent atmospheric waves, *J. Geophys. Res.* **121,** 10–157, doi: 10.1002/2016JA023226.

Godin, O. A., N. A. Zabotin, A. F. Sheehan, Z. Yang, and J. A. Collins (2013). Power spectra of infragravity waves in a deep ocean, *Geophys. Res. Lett.* **40,** no. 10, 2159–2165, doi: 10.1002/grl.50418.

Hanks, T. C., and H. Kanamori (1979). Moment magnitude scale, *J. Geophys. Res.* **84,** no. NB5, 2348–2350, doi: 10.1029/JB084iB05p02348.

Haran, T., M. Klinger, J. Bohlander, M. Fahrenstock, T. Painter, and T. Scambos (2018). MEaSUREs MODIS mosaic of Antarctica 2013-2014 (MOA2014) image map, Version 1, NSIDC: National Snow and Ice Data Center, Boulder, Colorado, doi: 10.5067/RNF17BP824UM.

Haubrich, R. A., W. H. Munk, and F. E. Snodgrass (1963). Comparative spectra of microseisms and swell, *Bull. Seismol. Soc. Am.* **53,** no. 1, 27–37.

Hell, M. C., B. D. Cornelle, S. T. Gille, A. J. Miller, and P. D. Bromirski (2019). Identifying ocean swell generation events from Ross Ice Shelf seismic data, *J. Atmos. Ocean. Tech.* **36,** no. 11, 2171–2189, doi: 10.1175/jtech-d-19-0093.1.

Hell, M. C., S. T. Gille, B. D. Cornuelle, A. Miller, P. Bromirski, and A. Crawford (2020). Estimating Southern Ocean storm positions with seismic observations, *J. Geophys. Res.* **125,** e2019JC015898, doi: 10.1029/2019JC015898.

Holdsworth, G., and J. Glynn (1978). Iceberg calving from floating glaciers by a vibrating mechanism, *Nature* **274,** no. 5670, 464–466.

Horgan, H. J., R. T. Walker, S. Anandakrishnan, and R. B. Alley (2011). Surface elevation changes at the front of the Ross ice shelf: Implications for basal melting, *J. Geophys. Res.* **116,** no. C2, doi: 10.1029/2010jc006192.

Hotovec-Ellis, A., S. Prejean, J. Vidale, and J. Gomberg (2012). Strongly gliding harmonic tremor during the 2009 eruption of Redoubt volcano, *J. Volcanol. Geoth. Res.* **259,** 89–99, doi: 10.1016/j.jvolgeores.2012.01.001.

Lazzara, M. A., K. C. Jezek, T. A. Scambos, D. R. Mac Ayeal, and C. J. V. D. Veen (2008). On the recent calving of icebergs from the Ross ice shelf, *Polar Geogr.* **31,** nos. 1/2, 15–26, doi: 10.1080/10889370802175937.

Lipovsky, B. (2018). Ice shelf rift propagation and the mechanics of wave induced fracture, *J. Geophys. Res.* **123,** 4014–4033, doi: 10.1029/2017JC013664.

Lipovsky, B., and E. Dunham (2015). Vibrational modes of hydraulic fractures: Inference of fracture geometry from resonant frequencies and attenuation, *J. Geophys. Res.* **120,** no. 2, 1080–1107.

Lipovsky, B., and E. Dunham (2016). Tremor during ice-stream stick slip, *Cryosphere* **10,** no. 1, 385–399.

MacAyeal, D., E. A. Okal, R. C. Aster, and J. N. Bassis (2008). Seismic and hydroacoustic tremor generated by colliding icebergs, *J. Geophys. Res.* **113,** no. F3, F03011, doi: 10.1029/2008jf001005.

MacAyeal, D., E. A. Okal, R. C. Aster, and J. N. Bassis (2009). Seismic observations of glaciogenic ocean waves (micro-tsunamis) on icebergs and ice shelves, *J. Glaciol.* **55,** no. 190, 193–206.

MacAyeal, D., E. Okal, R. Aster, J. Bassis, K. Brunt, L. M. Cathles, R. Drucker, H. A. Fricker, Y. J. Kim, S. Martin, *et al.* (2006). Transoceanic wave propagation links iceberg calving margins of Antarctica with storms in tropics and Northern Hemisphere, *Geophys. Res. Lett.* **33,** no. 17, L17502, doi: 10.1029/2006gl027235.

MacAyeal, D., T. Wang, and E. Okal (2015). Ambient seismic, hydroacoustic, and flexural gravity wave noise on a tabular iceberg, *J. Geophys. Res.* **120,** 200–211, doi: 10.1002/2014JF003250.

Martin, S., R. Drucker, R. Aster, F. Davey, E. Okal, T. Scambos, and D. MacAyeal (2010). Kinematic and seismic analysis of giant tabular iceberg breakup at Cape Adare, Antarctica, *J. Geophys. Res.* **115,** doi: 10.1029/2009JB006700.

Massom, R. A., T. A. Scambos, L. G. Bennetts, P. Reid, V. A. Squire, and S. E. Stam-Merjohn (2018). Antarctic ice shelf disintegration

Downloaded from http://pubs.geoscienceworld.org/ssa/srl/article-pdf/doi/10.1785/0220200478/5285507/srl-2020478.1.pdf
by Bradley Lipovsky

triggered by sea ice loss and ocean swell, *Nature* **558,** no. 7710, 383–389, doi: 10.1038/s41586-018-0212-1.

Nettles, M., and G. Ekstrom (2010). Glacial earthquakes in Greenland and Antarctica, *Annu. Rev. Earth Planet. Sci.* **38,** 467–491, doi: 10.1146/annurev-earth-040809-152414.

Okal, E. A., and D. MacAyeal (2006). Seismic recording on drifting icebergs: Catching seismic waves, tsunamis and storms from Sumatra and elsewhere, *Seismol. Res. Lett.* **77,** no. 6, 659–671.

Olinger, S., L. Bradley, D. Wiens, R. Aster, P. Bromirski, Z. Chen, P. Gerstoft, A. A. Nyblade, and R. A. Stephen (2019). Tidal and thermal stresses drive seismicity along a major Ross Ice Shelf rift, *Geophys. Res. Lett.* **46,** 6644–6652, doi: 10.1029/2019GL082842.

Paolo, F., H. A. Fricker, and L. Padman (2015). Volume loss from Antarctic ice shelves is accelerating, *Science* **348,** no. 6232, 327–331, doi: 10.1126/science.aaa0940.

Pattyn, F., and M. Morlighem (2020). The uncertain future of the Antarctic ice sheet, *Science* **367,** 1331–1335, doi: 10.1126/science.aaz5487.

Peng, Z., J. Walter, R. Aster, A. Nyblade, D. Wiens, and S. Anandakrishan (2014). Antarctic icequakes triggered by the 2010 Maule earthquake in Chile, *Nat. Geosci.* doi: 10.1038/ngeo2212.

Press, F., and M. Ewing (1951). Propagation of elastic waves in a floating ice sheet, *Eos Trans. AGU* **32,** no. 5, 673–678.

Press, F., A. Crary, J. Oliver, and S. Katz (1951). Air-coupled flexural waves in floating ice, *Eos Trans. AGU* **32,** no. 2, 166–172.

Scambos, T. A., T. M. Haran, M. A. Fahnestock, T. H. Painter, and J. Bohlander (2007). MODIS-based Mosaic of Antarctica (MOA) data sets: Continent-wide surface morphology and snow grain size, *Rem. Sens. Environ.* **111,** nos. 2/3, 242–257, doi: 10.1016/j.rse.2006.12.020.

Scambos, T. A., H. A. Fricker, C.-C. Liu, J. Bohlander, J. Fastook, A. Sargent, R. Massom, and A.-M. Wu (2009). Ice shelf disintegration by plate bending and hydro-fracture: Satellite observations and model results of the 2008 Wilkins Ice Shelf break-ups, *Earth Planet. Sci. Lett.* **280,** 51–60, doi: 10.1016/j.epsl.2008.12.027.

Van der Veen, C. (1998). Fracture mechanics approach to penetration of surface crevasses on glaciers, *Cold Reg. Sci. Tech.* **27,** no. 1, 31–47.

Wagner, T. J. W., P. Wadhams, R. Bates, P. Elosegui, A. Stern, D. Vella, E. P. Abrahamsen, A. J. Crawford, and K. W. Nicholls (2014). The footloose mechanism: Iceberg decay from hydrostatic stresses, *Geophys. Res. Lett.* **41,** no. 15, 5522–5529, doi: 10.1002/2014gl060832.

Wessel, P., and W. H. F. Smith (1998). New, improved version of generic mapping tools released, *Eos Trans. AGU* **79,** no. 47, 579–579, doi: 10.1029/98EO00426.

Winberry, J. P., A. D. Huerta, S. Anandakrishnan, R. Aster, A. Nyblade, and D. A. Wiens (2020). Glacial earthquakes and precursory seismicity associated with Thwaites Glacier calving, *Geophys. Res. Lett.* doi: 10.1029/2019gl086178.

Yamada, T., J. J. Mori, S. Ide, R. E. Abercrombie, H. Kawakata, M. Nakatani, Y. Lio, and H. Ogasawara (2007). Stress drops and radiated seismic energies of microearthquakes in a South African gold mine, *J. Geophys. Res.* **112,** no. B3, doi: 10.1029/2006jb004553.

Zhan, Z., V. C. Tsai, J. Jackson, and D. Helmberger (2014). Ambient noise correlation on the Amery Ice Shelf, East Antarctica, *Geophys. J. Int.* **196,** 1796–1802, doi: 10.1093/gji/ggt488.

Zhuchkova, M. G., and D. P. Kouzov (2012). Resonance effects in propagation of flexural-gravity waves for a supported elastic plate floating on water, *2012 Proc. of the Int. Conf. Days on Diffraction*, 253–258, doi: 10.1109/DD.2012.6402791.

Appendix

The Dirac comb

For a time series of repeating subevents with uniform interevent times τ, the spectrum calculated over a time window that is much greater than τ will necessarily exhibit harmonic spectral peaks. In the limit of a perfectly periodic time series, the theoretical spectrum will approach a harmonic sequence of delta functions or, equivalently, can be represented by a Fourier series (e.g., Bracewell, 1986). Tremor-like seismic signals have been previously attributed to this repeating subevent effect in glaciological (MacAyeal *et al.*, 2008; Lipovsky and Dunham, 2016) and volcanological (Hotovec-Ellis *et al.*, 2012) processes.

If each subevent has a time series $g(t)$ and repeats at an interval τ, then the full time series $\phi(t)$ can be represented as the infinite series:

$$\phi(t) = g(t) * \tau^{-1}\mathrm{III}(t/\tau) = \sum_{n=-\infty}^{\infty} g(t - n\tau), \tag{A1}$$

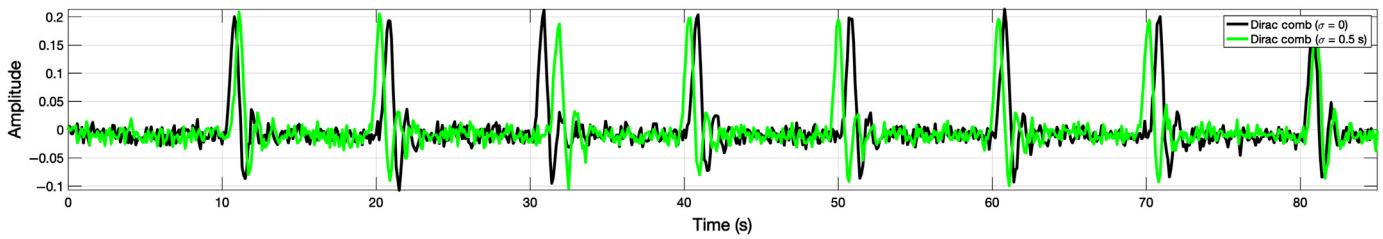

Figure A1. Dirac comb example synthetic nonrandomized (black) and randomized (green) time-series realizations with a sampling rate of 10 Hz. Impulsive subevents (amplitude A) in the nonrandomized time series (with origin times at 10, 20, …, s) are randomized by independent zero-mean normal timing variations with $\sigma = 0.5$ s. Both realizations incorporate low-amplitude ($\sigma_n = A/100$) uncorrelated white noise. Subevent waveforms $g(t)$ are unit impulse functions filtered with a (causal) eight-pole low-pass Butterworth filter and a corner frequency of 1 Hz. The color version of this figure is available only in the electronic edition.

Downloaded from http://pubs.geoscienceworld.org/ssa/srl/article-pdf/doi/10.1785/0220200478/5285507/srl-2020478.1.pdf
by Bradley Lipovsky

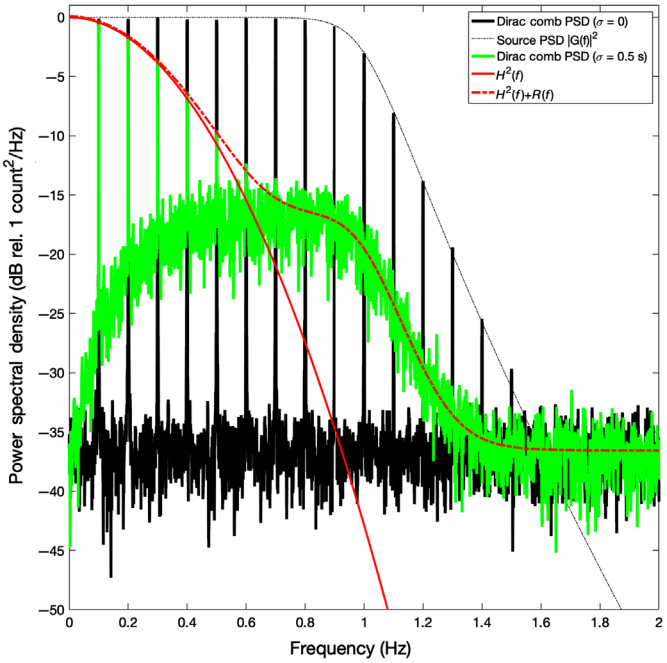

Figure A2. Normalized (zero dB at zero frequency) power spectral densities (PSDs) for the synthetic time-series realization of Fig. A1. Black and green spectra are numerically calculated spectra for constant and randomized interevent timing, respectively. Black envelope function is the PSD of the subevent source. Red curves indicate theoretical envelope functions described earlier as identified in the legend. Both realizations incorporate $\sigma_n = A/100$ uncorrelated Gaussian white noise, which determines the PSD floor of $\Phi_n \approx -36$ dB. The color version of this figure is available only in the electronic edition.

in which $*$ denotes convolution, and III is the Dirac comb or shah function; an infinite sequence of unit weight delta functions occurring at integer times. It can be shown by taking a limit series of narrowing Gaussian pulses (Bracewell, 1986) that the Fourier transform of III is

$$\tau^{-1}\int_{-\infty}^{\infty} \mathrm{III}(t/\tau)e^{-\imath 2\pi f t}dt = \mathrm{III}(f\tau). \tag{A2}$$

The Fourier transform of $\phi(t)$ is, by the convolution theorem,

$$\Phi(f) = G(f)\,\mathrm{III}(f\tau), \tag{A3}$$

in which $G(f)$ is the Fourier transform of $g(t)$.

We introduce normally distributed randomness in the interevent times for a sequence of repeating events, by considering subevent times $n\tau + \sigma Z$, in which n is an integer, $\sigma \ll \tau$ is the standard deviation of interevent time variation, and Z is the zero-mean standard normal random variable. For a discrete time series of length N composed of numerous subevents, the expected value of the corresponding spectral peak envelope at Fourier transform frequency index k can be found from the expected value calculation:

$$H(k) = E[e^{\Theta Z}], \tag{A4}$$

in which $\Theta = -\imath 2\pi\sigma k/N$.

We then have

$$E[e^{\Theta Z}] = \int_{-\infty}^{\infty} e^{\Theta z}\frac{1}{\sqrt{2\pi}}e^{-z^2/2}dz, \tag{A5}$$

$$= \frac{1}{\sqrt{2\pi}}\int_{-\infty}^{\infty} e^{-(z^2+2\Theta z)/2}dz. \tag{A6}$$

Completing the square within the exponent produces

$$E[e^{\Theta Z}] = e^{\Theta^2/2}\int_{-\infty}^{\infty}\frac{1}{\sqrt{2\pi}}e^{-(z+\Theta)^2/2}dz, \tag{A7}$$

$$= e^{\Theta^2/2}(1), \tag{A8}$$

$$= e^{-2\pi^2\sigma^2k^2/N^2}. \tag{A9}$$

Transforming to continuous time and frequency, and substituting $k/N = f/f_s$ produces

$$H(f) = e^{-2\pi^2\sigma^2f^2/f_s^2}, \tag{A10}$$

in which f_s is the sampling rate.

The effect of normally distributed independent variation in subevent times on the periodic components of the Dirac comb spectrum is, thus, to multiply the nonrandomized Dirac comb spectrum (equation A2) by $H(f)$ (equation A10), which reduces the amplitudes of the higher harmonics. In the limit of higher frequencies, in which the randomization of an impulse series will produce no spectral lines, the spectrum asymptotically approaches that of a white process, for which with the (constant and one-sided) power spectral density (PSD) expected value is

$$Q = \frac{2P_w}{f_s}, \tag{A11}$$

in which

$$P_w = \frac{1}{N}\sum_{i=1}^{N}\phi_i^2, \tag{A12}$$

Downloaded from http://pubs.geoscienceworld.org/ssa/srl/article-pdf/doi/10.1785/0220200478/5285507/srl-2020478.1.pdf
by Bradley Lipovsky

is the average power of the time series, in which ϕ_i is the sampled $\phi(t)$ (equation A1).

The full expression for the expected value of the randomized interevent time Dirac comb PSD for an unfiltered sequence of impulses is thus

$$S(f) = H^2(f)\Phi_{\mathrm{III}}(f) + Q, \tag{A13}$$

in which $\Phi_{\mathrm{III}}(f)$ is the PSD of the nonrandomized Dirac comb.

More generally, for identical nonimpulse time functions, $g(t)$ with spectra $G(f)$ and a background noise spectral density Φ_n, the expected value of the PSD for the randomized interevent time Dirac comb becomes

$$S(f) = H^2(f)\Phi_{\mathrm{III}}(f) + R(f), \tag{A14}$$

in which

$$R(f) = W(f)|G(f)|^2 + \Phi_n, \tag{A15}$$

and $W(f)$ is the prewhitened average signal PSD. Because the pre-whitened time series is a sequence of M impulses of amplitude A with mean time separations of τ samples, the expected value of the (one-sided) PSD is given by distributing this energy uniformly with frequency (as for randomized interevent times).

$$W(f) = 2\frac{A^2}{\tau f_s^2}. \tag{A16}$$

We note that the interevent timing standard deviation σ may be estimated from the harmonic normalized PSD envelope $H^2(f)$, using equation A10 under these assumptions. The MATLAB code used to produce two figures in this appendix is included in the supplemental material to this article as Appendix C.

Manuscript received 28 December 2020
Published online 21 April 2021

Downloaded from http://pubs.geoscienceworld.org/ssa/srl/article-pdf/doi/10.1785/0220200478/5285507/srl-2020478.1.pdf
by Bradley Lipovsky